Landsvirkjun

LV-2025-006

2002–2023 ground displacements and strain in the Þeistareykir and Krafla areas based on GNSS and InSAR

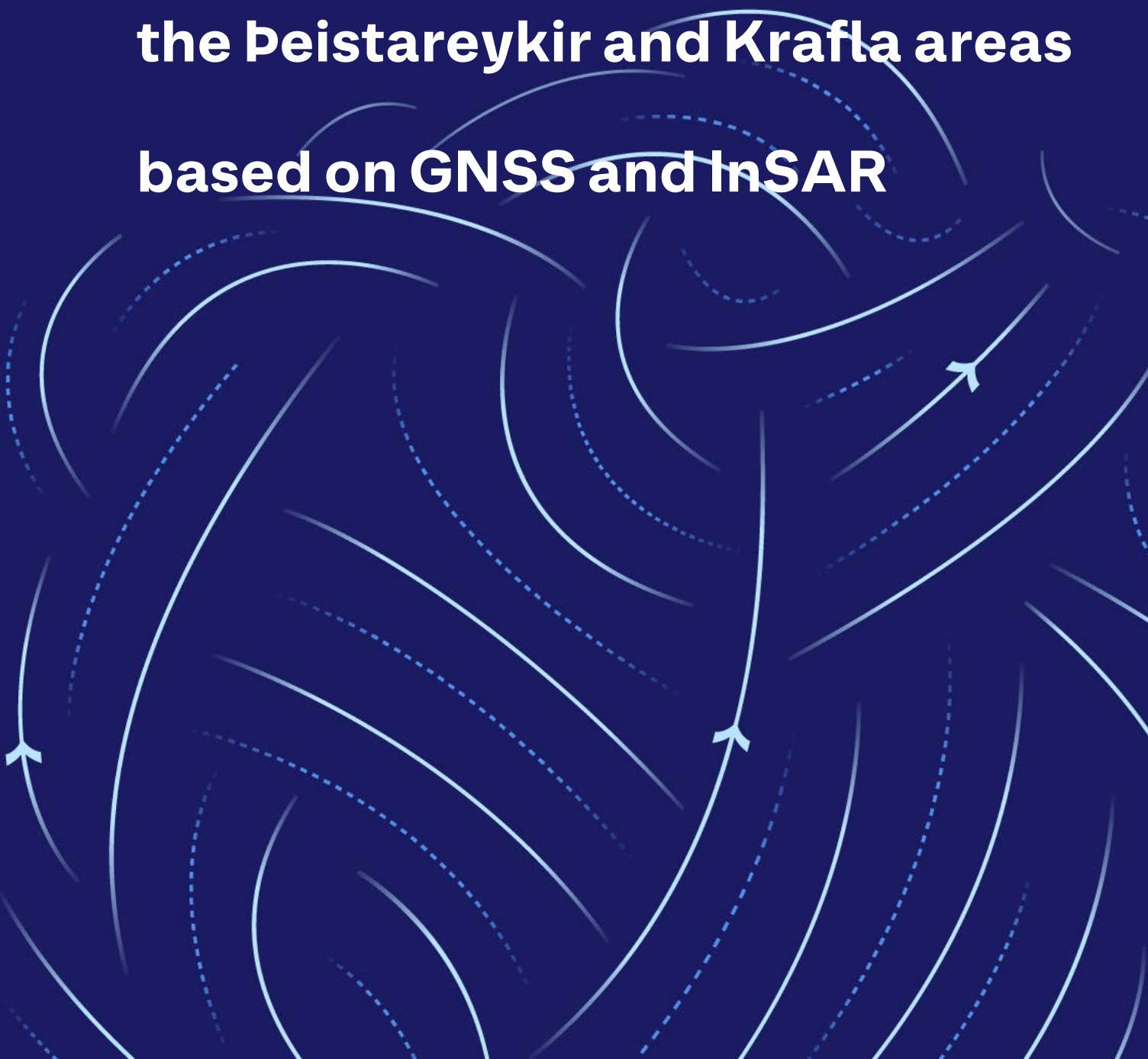

2002–2023 ground displacements and strain in the Þeistareykir and Krafla areas based on GNSS and InSAR

Höfundur
Yilin Yang[1]
Freysteinn Sigmundsson[1]
Vincent Drouin[2]
Halldór Geirsson[1]

1 Nordic Volcanological Center, Institute of Earth Sciences, University of Iceland

2 Icelandic Meteorological Office

Dagsetning
January 2025

Lykilsíða

Skýrsla LV nr	LV-2025-006 RH-05-2024	**Dagsetning**	January 2025
Fjöldi síðna	57	**Upplag**	1
Dreifing	[ ] Birt á vef LV	[X] Opin	[ ] Takmörkuð til [Dags.]
Titill	2002–2023 ground displacements and strain in the Þeistareykir and Krafla areas based on GNSS and InSAR		
Höfundar/fyrirtæki	Yilin Yang[1], Freysteinn Sigmundsson[1], Vincent Drouin[2], Halldór Geirsson[1] (1) Nordic Volcanological Center, Institute of Earth Sciences, University of Iceland (2) Icelandic Meteorological Office		
Verkefnisstjóri	Anette Kærgaard Mortensen		
Unnið fyrir	Landsvirkjun		
Samvinnuaðilar	–		
Útdráttur	This report evaluates ground displacements in the 2002–2023.9 period in the Þeistareykir and Krafla areas, with the aim to infer the average long-term velocity field not affected by episodic and transient motion. The areas are within the North American-Eurasian plate boundary deformation zone in the Northern Volcanic Zone of Iceland, where the plates are separating by 17.4 mm/yr in direction 292°. Regional deformation is dominated by stretching across the Krafla and Þeistareykir volcanic systems affecting conditions in their geothermal systems, where the geothermal energy is exploited. Ongoing glacial isostatic adjustment also influences the areas. This report evaluates the average long-term crustal velocity field in the 2002–2023.9 period based on available observations and analyzes corresponding strain rates. Focus is on the Þeistareykir area, and how the plate-boundary extension varies across the area, with possible involvement of fault movements and localized deformation.		
Lykilorð	Krafla, KRA, Þeistareykir, THR, ground displacement, geothermal, GNSS, InSAR		

Samþykki verkefnisstjóra Landsvirkjunar

Anette K. Mortensen

List of figures

Introduction

This report evaluates ground displacements in the 2002–2023.9 period in the Þeistareykir and Krafla areas, with the aim to infer the average long-term velocity field not affected by episodic and transient motion. The areas are within the North American-Eurasian plate boundary deformation zone in the Northern Volcanic Zone of Iceland, where the plates are separating by 17.4 mm/yr in direction 292° according to previous research on the displacement during 2008–2014 (Drouin et al., 2016). Regional deformation is dominated by stretching across the Krafla and Þeistareykir volcanic systems affecting conditions in their geothermal systems, where the geothermal energy is exploited. Ongoing glacial isostatic adjustment also influences the areas.

Other processes such as inter-seismic/aseismic fault movements, and steady volcanic-geothermal activities can cause long-term (>10 year) ground displacements with relatively steady rate. Multiple processes may deform the ground over shorter periods, leading to transient ground displacements. Investigating the long-term ground displacement not only enhances our understanding on these long-term processes, but also lays important basis for precisely monitoring other dynamic processes. This report evaluates the average long-term crustal velocity field in the 2002–2023.9 period based on available observations and analyzes corresponding strain rates. Particular focus is on the Þeistareykir area, and how the plate-boundary extension varies across the area, with possible involvement of fault movements and localized deformation.

Data and methodology

Global navigation satellite system (GNSS) uses ranging measurements from the Earth's surface to satellites for positioning and has become a powerful tool for monitoring ground displacements with millimeter-level precision. Continuous GNSS (cGNSS) usually records the site coordinates every day and campaign GNSS measures sites episodically (Freymueller, 2017). Long-term observation of both cGNSS and campaign GNSS derives time series for displacement velocity estimation.

Interferometric Synthetic Aperture Radar (InSAR) utilizes the phase difference between two SAR acquisitions to derive ground displacements. Although topography, satellite orbits, ground displacements, meteorological

conditions affect the observations and interpretations, InSAR time series analysis allows one to estimate the long-term ground displacements in the line-of-sight (LOS) direction of the satellite.

This report utilizes GNSS coordinate time series spanning 2002–2023 and InSAR averaged velocity field during 2017–2023 to investigate the long-term displacement in the Þeistareykir and Krafla areas. Detailed strategies for data processing are described by Lanzi et al. (2020), Yang et al. (2023), Drouin (2022) and references therein.

GNSS time series are analyzed to estimate the ground velocity field. As discretized GNSS velocity field only provides information at the site locations, spatially continuous displacement and strain maps are be obtained by different interpolation methods. Displacement and strain maps can also be obtained by combining the spatially discrete GNSS station velocities and InSAR line-of-sight displacement map.

The velocities of GNSS coordinate time series are calculated with least square estimation. For cGNSS time series, the linear velocities are estimated together with annual and semi-annual cycle of displacements (Blewitt & Lavallée, 2003). For campaign GNSS time series only linear velocities are estimated as the annual and semi-annual cycles of displacements are eliminated by taking the measurements at similar period every year. Due to the influence of transient processes, the linear velocities in the time series may change over time. Manual visual detection of the GNSS time series in the area suggests eventual velocity change during 2012 and/or 2013. Therefore, velocities spanning 2002.0–2013.0, 2013.0–2023.9 and 2002.0–2023.9 are estimated for all time series when data is available. If the velocity difference between 2002.0–2013.0 and 2013.0–2023.9 is smaller than 0.5 mm/yr the velocity spanning 2002.0–2023.9 is taken as the long-term velocity at the site, otherwise the velocity spanning 2013.0–2023.9 or site-customized data span is applied (see Figure 5 and Table 1).

Four interpolation methods are adopted in this report. The horizontal (east and north component) displacements are interpolated with algorithm GPSGridder implemented in the Generic Mapping Tools (GMT) software (Sandwell & Wessel, 2016). GPSGridder is a physics-based interpolation, based on the idea that observed displacements can be approximated to be the result of forces acting within an elastic body, the uppermost crust. The method finds a set of effective forces inside a thin elastic plate that reproduces observed velocities at the GNSS

stations and predicts velocities between the GNSS stations. It couples the two components of horizontal displacement considering elastic behavior of with an effective Poisson's ratio. The effective Poisson's ratio controls how strong the two components are coupled. During the inversion, the smoothness of the derived velocity field can be adjusted. For the larger area of Þeistareykir and Krafla, the effective Poisson's ratio is set to 0.25 and the minimum ratio between the largest eigenvalue and the rest is set to 1×10^{-5}. For the Þeistareykir area, the minimum ratio between the largest eigenvalue and the rest is changed to 1×10^{-7}.

The vertical displacements are interpolated with Kriging method, where a so-called variogram function is first fitted to represent the spatial covariance structure of observations and then applied as weights for interpolation. Kriging is a purely data-driven method.

The strain maps here are generated by an algorithm so-called velocity interpolation for strain rate (VISR; Shen et al., 2015). This method considers the distances between the interpolated point and the data points, as well as the spatial coverage of the data points, for weighting in the least square inversion of the local strain. It is chosen rather than inferred strain from the GPSGridder results, as GPSGridder derived strain maps can present singularities at the location of GNSS stations.

The combination of discretized GNSS velocities and InSAR displacement maps is here realized with the 'Simultaneous and Integrated Strain Tensor Estimation from geodetic and satellite deformation Measurements' (SISTEM) software (Guglielmino et al., 2011). This method avoids the interpolation of GNSS velocity field and obtains the displacement and strain map with the neighboring displacement observations of each grid and the gradient of a strain tensor. Estimated uncertainties of GNSS velocities are input for weighting and the uncertainty of InSAR displacement is set to 0.5 mm/yr (one value for all) to accommodate the GNSS velocity uncertainties and achieve proper weight of InSAR displacements. The socalled locality denominator, which is used for the normalization of spatial weight parameter, is set to 5.

Results

This report provides a series of maps and figures illustrating the GNSS and InSAR observations in the Þeistareykir and Krafla areas and their derived long-

term displacements and strain. Basic information of GNSS sites in the areas and data availability are shown in Figure 1 – Figure 3. Examples of GNSS coordinate time series in Figure 4 illustrate possible velocity change in the displacement velocities. Figure 5 gives an illustration of GNSS time series analysis strategy to obtain reliable displacement velocity estimates. Discretized GNSS velocity fields in different components and areas are shown in Figure 6, Figure 9, Figure 14 and Figure 16. Their interpolated GNSS displacement maps are shown in Figure 7, Figure 8, Figure 10, Figure 11, Figure 12, Figure 13 Figure 15, Figure 17 and Figure 18. Figure 19 and Figure 20 show strain maps derived from discretized GNSS velocity field. The yearly averaged InSAR displacement maps are shown in Figure 21 – Figure 23. The combined displacement maps from discretized GNSS velocity field and InSAR displacement maps with SISTEM are shown in Figure 24 – Figure 29 and Figure 32 – Figure 34. Its corresponding 2D areal strain maps are shown in Figure 30 – Figure 31. Then Figure 35 – Figure 39 analyze the profiles of displacement across the Þeistareykir area.

The long-term GNSS interpolated displacement maps and inferred crustal velocity fields show that horizonal velocities do mostly vary gradually across the plate boundary in the Þeistareykir and the Krafla areas. Relative to Eurasia plates, the east-component velocity ranges from ~-2 mm/yr in the east (approaching the estimated velocity of stable Eurasian plate interior, that would be zero) to <-20 mm/yr in the west (approaching the velocity of the north American plate). North-component velocity ranges from ~-2 mm/yr in the east to >10 mm/yr in the west. Local small-scale variations of velocities are evident mainly in the Krafla caldera as well as the central and the eastern of the Þeistareykir central volcano.

Across the Þeistareykir area from east to west, the east-component velocity changes from ~-5 mm/yr to ~-15 mm/yr and north-component velocity changes from ~0 mm/yr to ~7 mm/yr. The area with velocity of ~6 mm/yr in the north component extends further east than in the surrounding areas in the central part of the Þeistareykir. Two GNSS sites east of the Þeistareykir show larger east-component velocities (-8–-9 mm/yr) than the surrounding stations (~-10 mm/yr).

The vertical GNSS velocities reveal three areas of subsidence compared to a background regional uplift of ~2 mm/yr. Those are, (i) the western coast of Tjörnes, (ii) the northen half of the Þeistareykir central volcano to the southern extension of the Husavik-Flatey Fault, (iii) central Krafla caldera to a more extended area of Námafjall and Hverfjall.

The strain map obtained with GNSS observation is consistent with the vertical displacement with subsidnece area (iii) in the Krafla volcanic system having a contraction of several hundred nanostrain/yr. Subsidence area (ii) in the Þeistareykir volcano has indication of slight contraction of <100 nanostrain/yr.

The combined displacement and strain maps from GNSS and InSAR show similar charateristics on a large scale (across the plate boundary) as the GNSS-only displacement maps, but reveal also more local features. For instance, the faster northward movement (~8 mm/yr) in southwest of the Þeistareykir central volcano than that to the northeast (2–4 mm/yr), and the significant decrease (~1 mm/yr) of north-component velocity in central Krafla caldera. However, some features should be taken carefully due to artifacts from topography.

Four profiles are evaluated across the Þeistareykir central volcano, which indicates again the consistency between GNSS-only displacement maps and those combing GNSS and InSAR observations. No significant displacement anomalies are evident at faults or fractures on the profiles, except an area of subsidence more than -3 mm/yr in the middle of the central-north profile, that is, the northwest to the Bæjarfjall. This has been reported in previous observation (Drouin, 2023; Yang, 2023), and may relate to the geothermal exploitation.

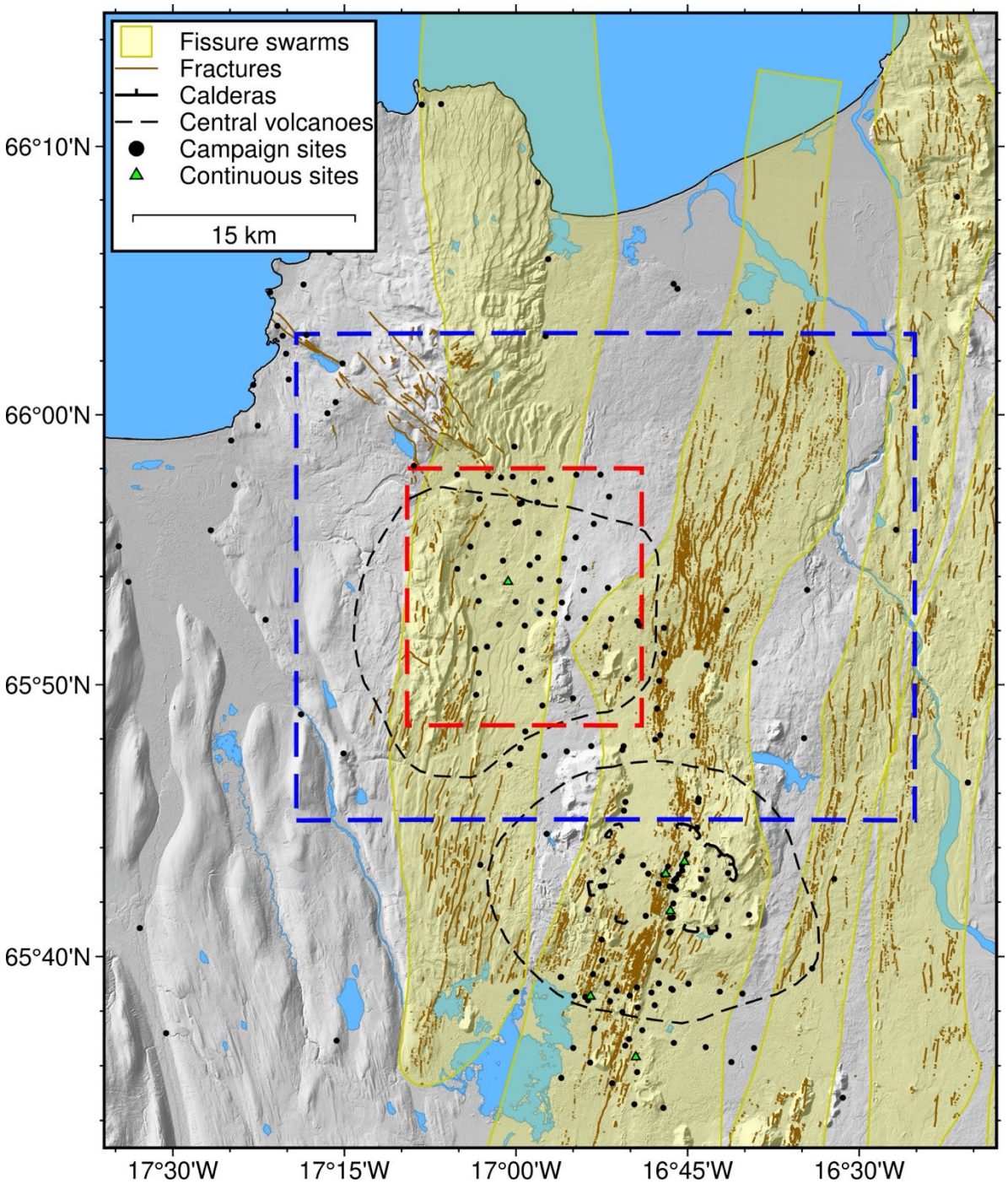

Figure 1. Map of GNSS sites in the Þeistareykir and Krafla areas. Shaded topography is from LMI (2022) and fractures are from Hjartardóttir et al. (2015); shown in all the figures. The blue rectangle with dashed lines indicates the area of Þeistareykir shown in Figure 2. The red rectangle with dashed lines indicates a smaller area of Þeistareykir with displacement variations as shown in Figure 12, Figure 13, Figure 18, and Figure 32 – Figure 34.

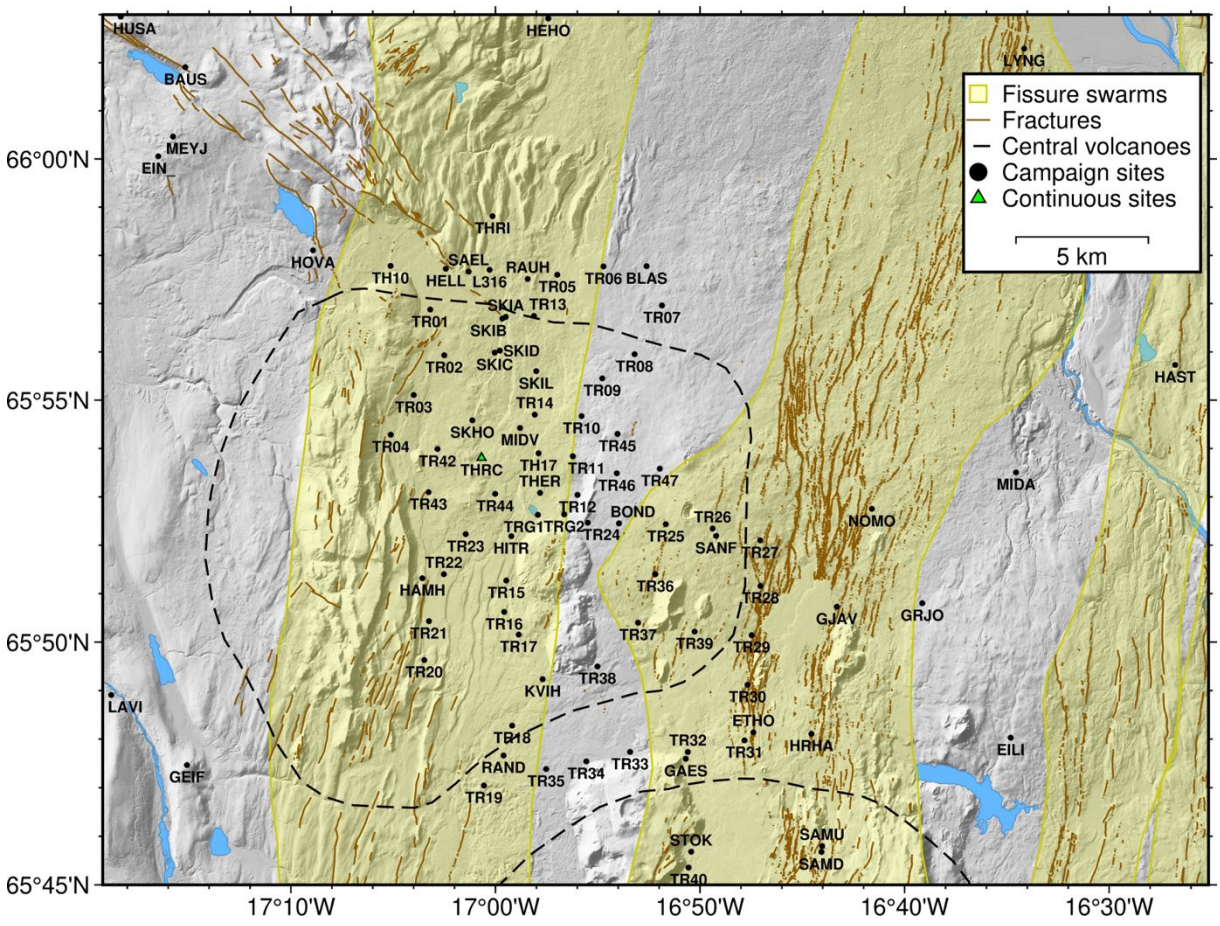

Figure 2. Map of GNSS sites in the Þeistareykir area. Site names are shown next to each station symbol (filled circles and triangles).

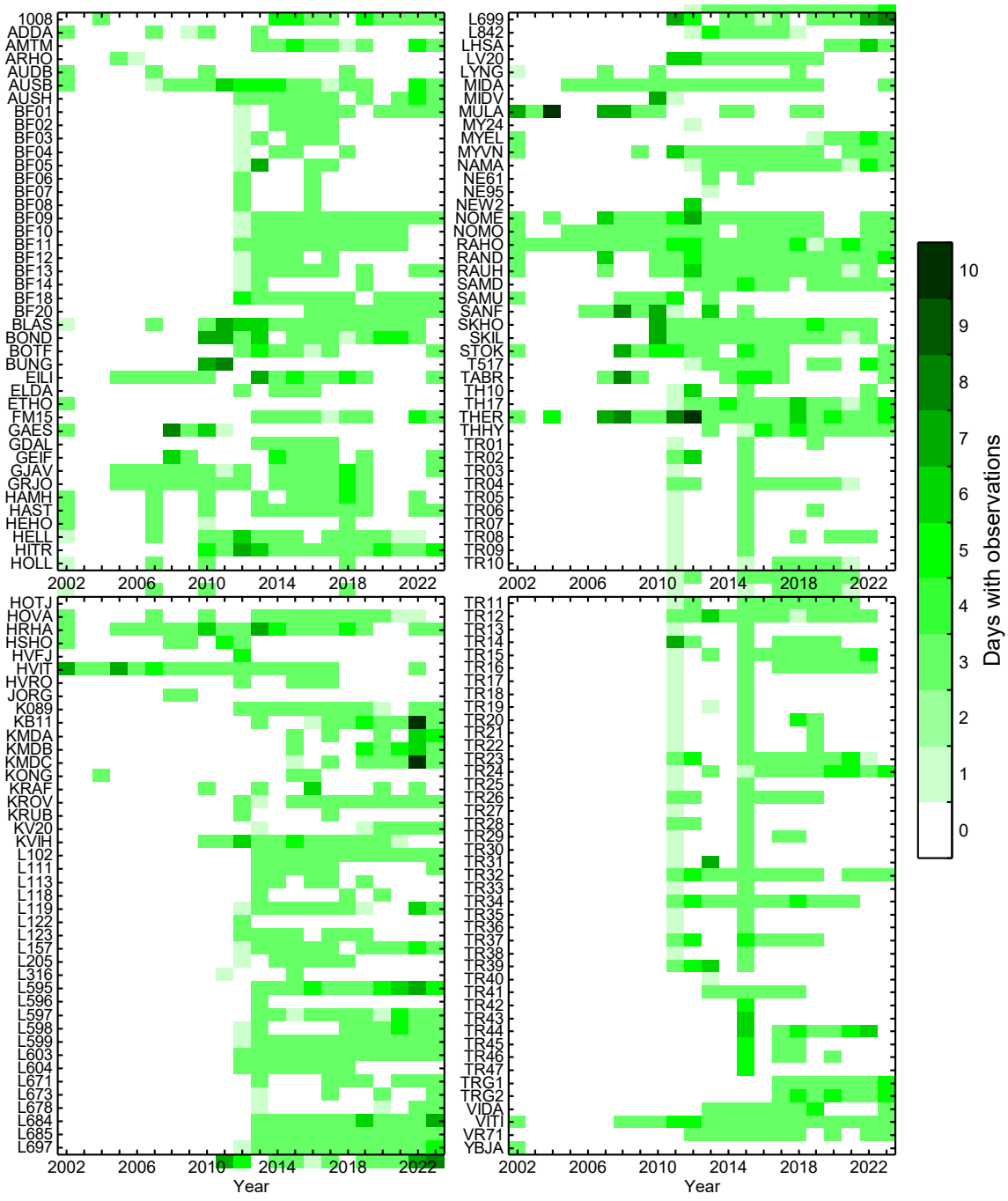

Figure 3. Summary of campaign GNSS data available. The color codes indicate how many days of observation each campaign site has in different years. The site names starting with TR are located in the Þeistareykir area, with first measurements in 2011.

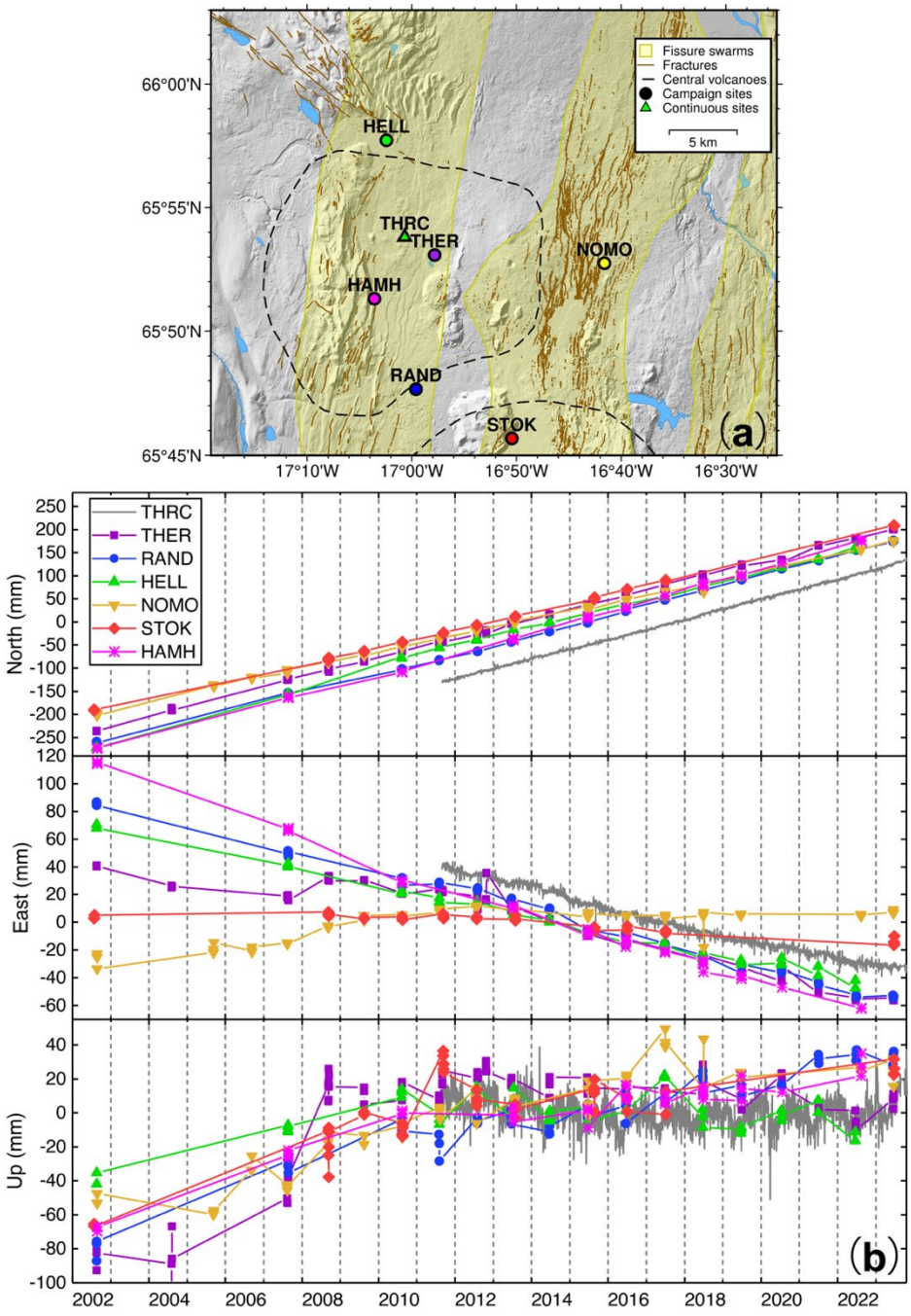

Figure 4. Examples of GNSS coordinate time series from the Þeistareykir area. (a) The locations of the selected GNSS sites in the Þeistareykir area. (b) GNSS coordinate time series at selected GNSS sites. The coordinates are relative to IGb14/ITRF2014 (Altamimi et al., 2016). Sites THER, RAND and HAMH exemplify displacements in the central, southern, and western parts of the Þeistareykir central volcano, respectively. Sites HELL and NOMO exemplify the displacements to the north and west of the Þeistareykir central volcano, respectively. Site STOK exemplifies the displacement in the Krafla central volcano.

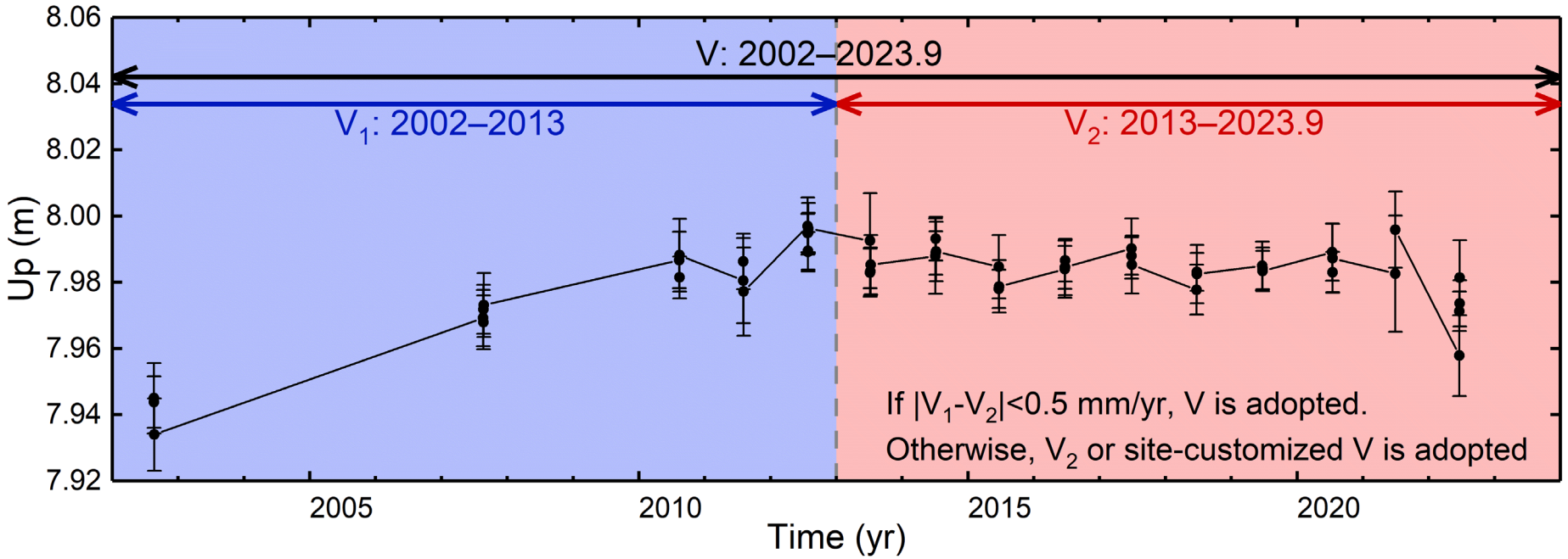

Figure 5. Illustration of GNSS time series analysis strategy for displacement velocity estimation. The exemplified time series is the up component at site RAUH. V represents displacement velocity.

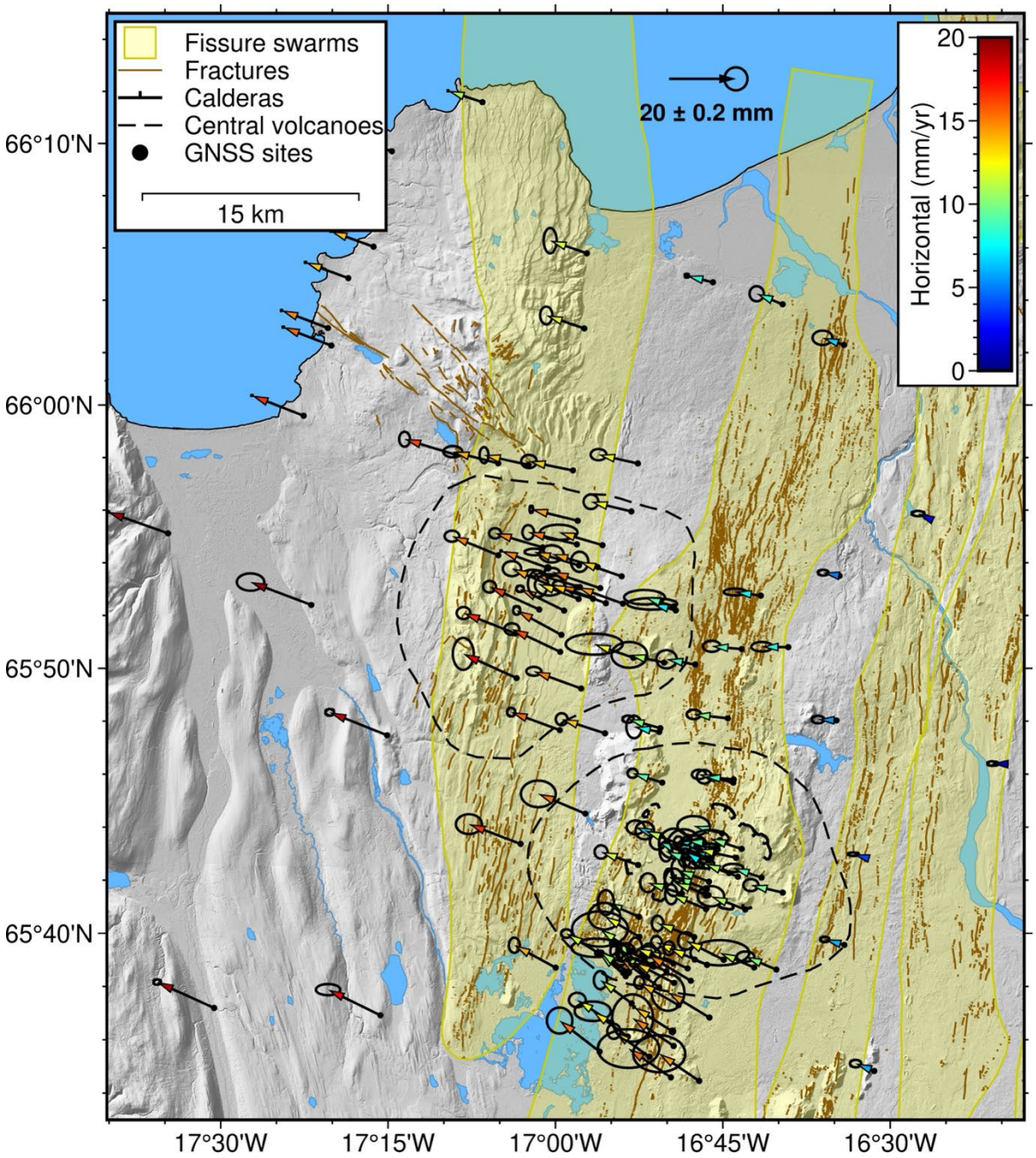

Figure 6. GNSS horizontal displacement velocity field in the Þeistareykir and Krafla areas. The velocities are referred to Eurasian plate based on the ITRF2014 plate motion model (Altamimi et al., 2017). The ellipsoids indicate the uncertainties of velocity estimates (standard deviation, ~68% confidence interval). The arrows are color-coded according to the magnitude of horizontal velocities. The time span of GNSS time series used to derive the velocity field is explained in the text.

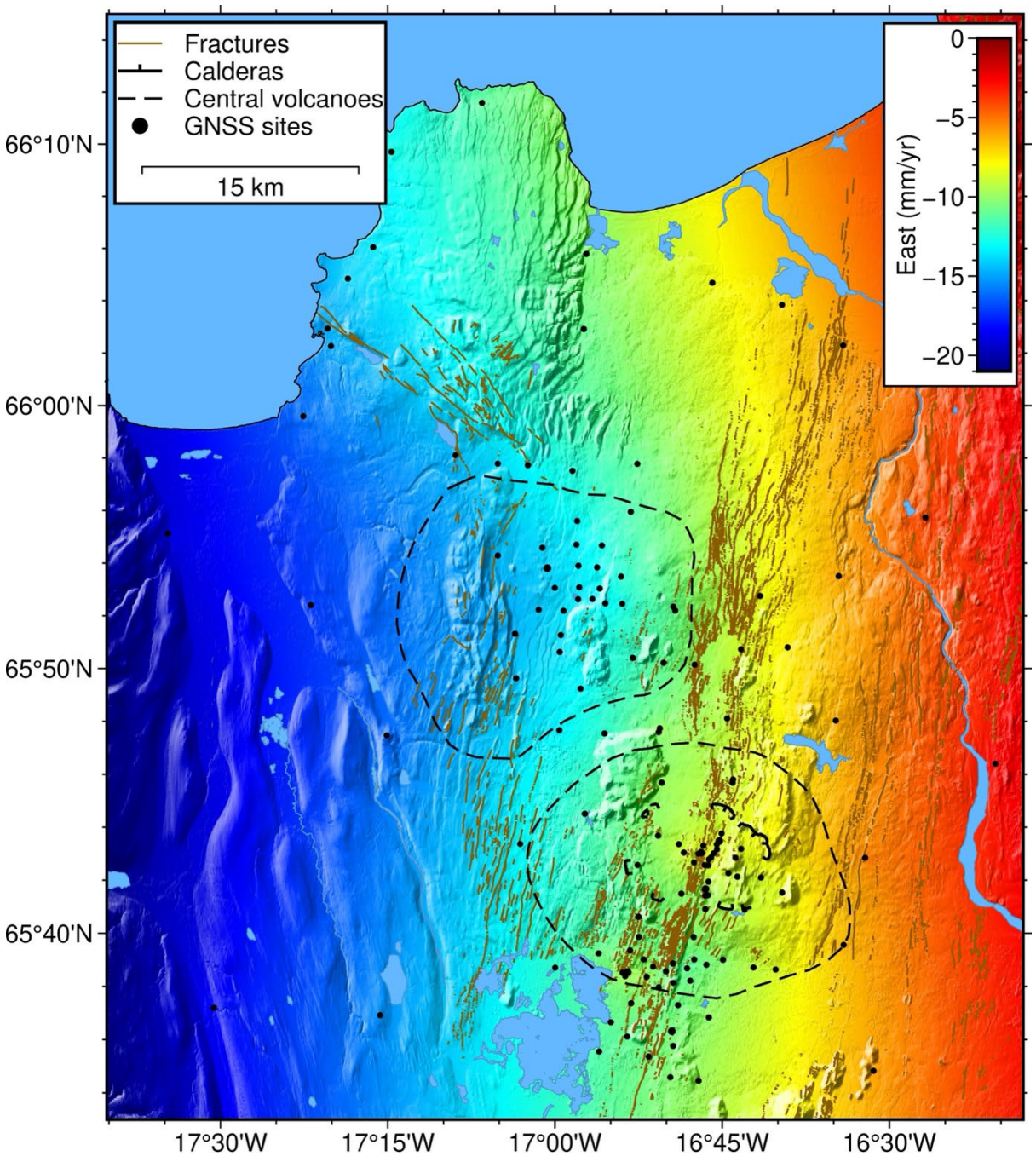

Figure 7. Interpolated GNSS east-component displacement velocity field in the Þeistareykir and Krafla areas. The interpolation method is algorithm GPSGridder implemented in Generic Mapping Tools (GMT). See the text for the explanation of parameters.

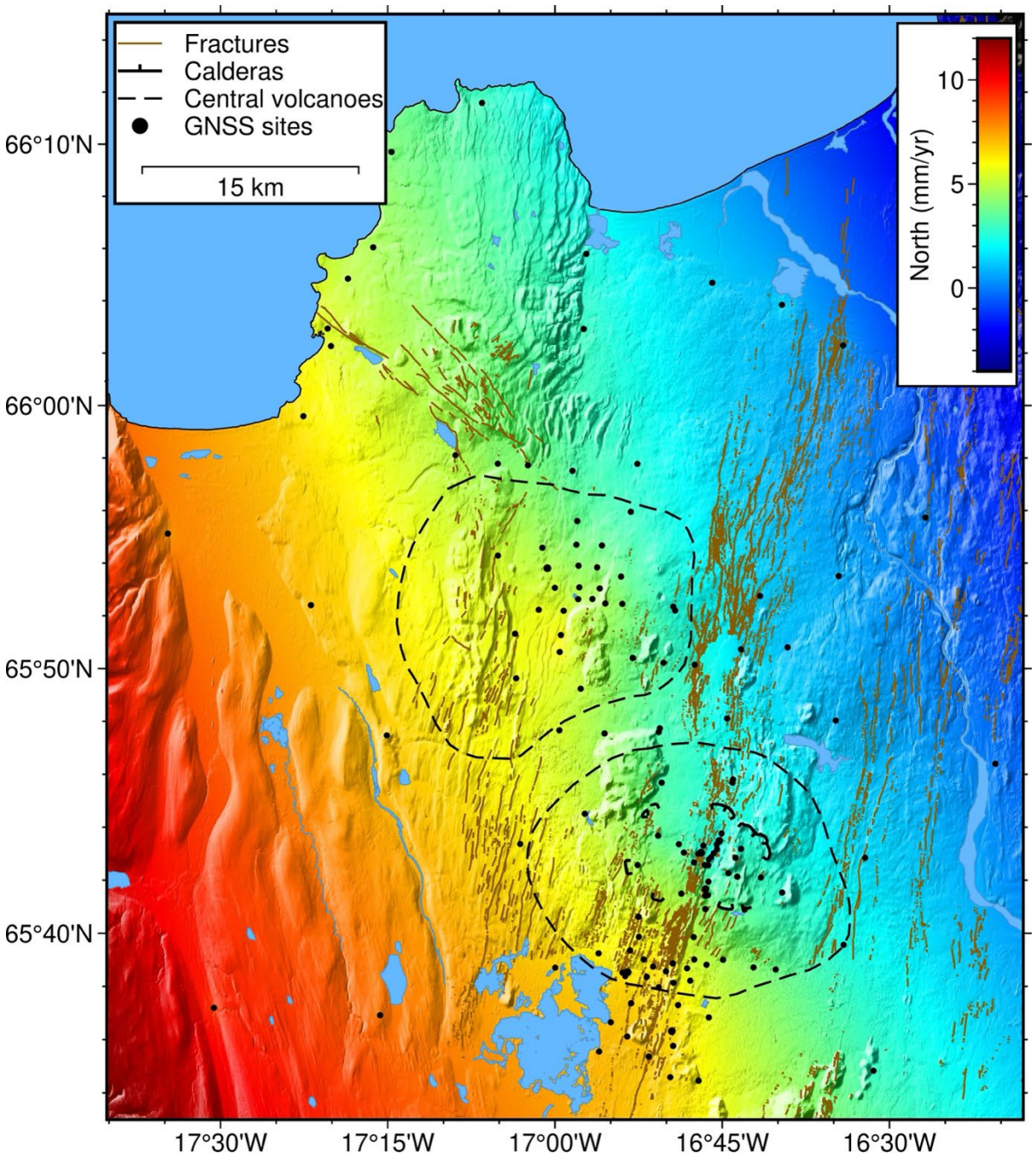

Figure 8. Interpolated GNSS north-component displacement velocity field at the Þeistareykir and Krafla areas. The interpolation method is algorithm GPSGridder implemented in Generic Mapping Tools (GMT). See the text for the explanation of parameters.

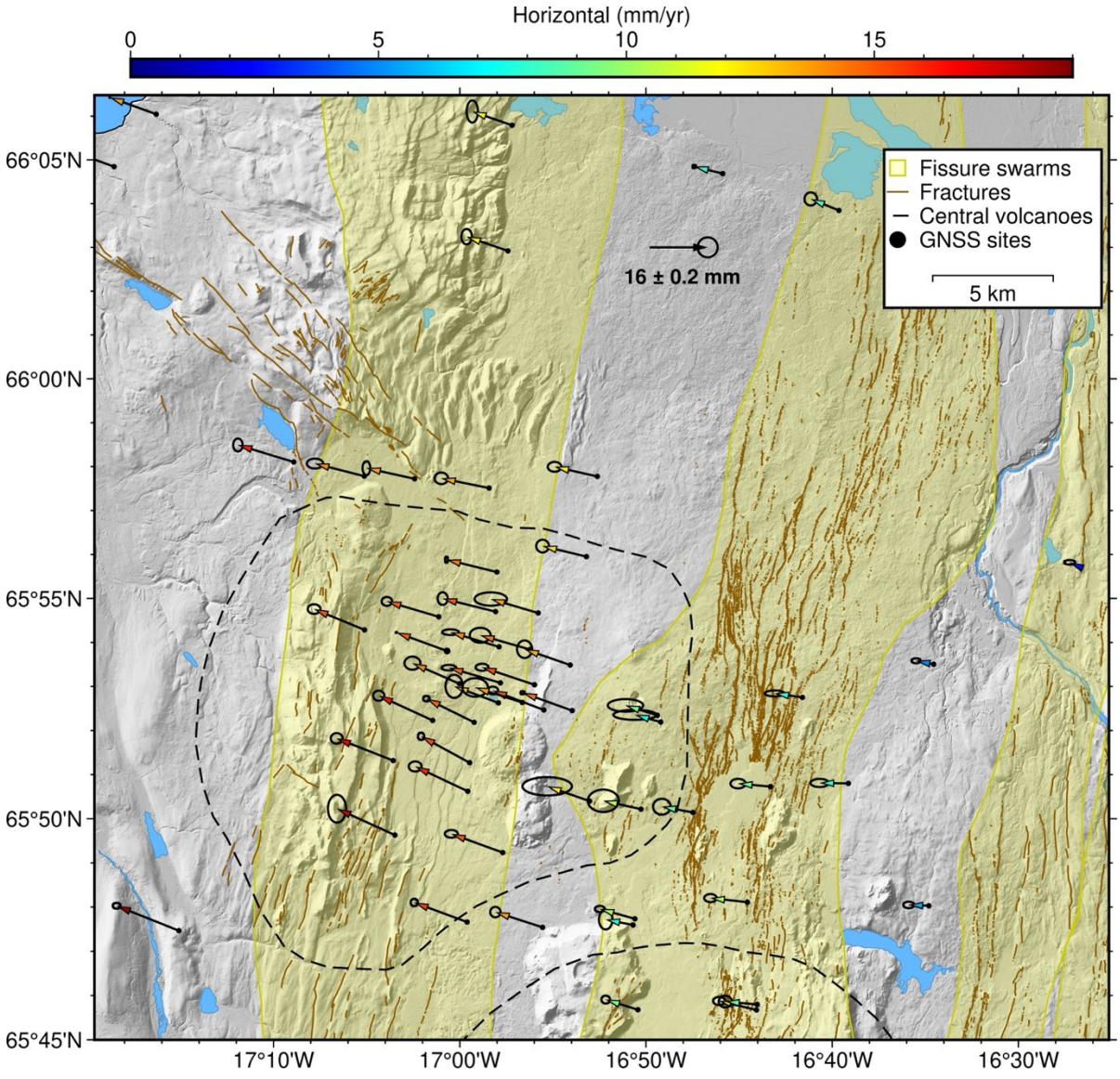

Figure 9. GNSS horizontal displacement velocity field at the Þeistareykir area. The velocities are referred to Eurasian plate based on the ITRF2014 plate motion model (Altamimi et al., 2017). The ellipsoids indicate the uncertainties of velocity estimates (standard deviation, ~68% confidence interval). The arrows are color-coded according to the magnitude of horizontal velocities. The time span of GNSS time series deriving the velocity field is explained in the text.

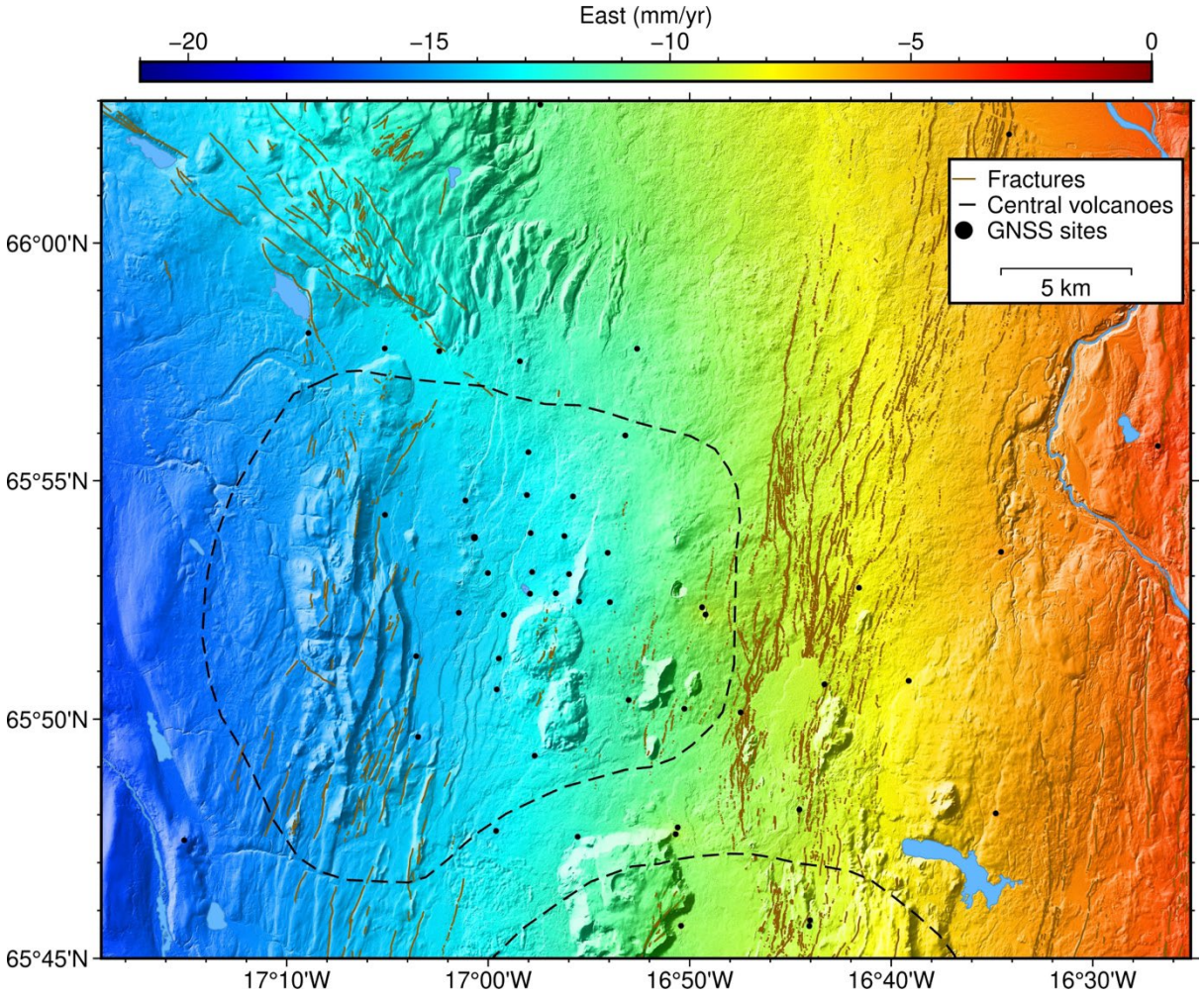

Figure 10. Interpolated GNSS east-component displacement velocity field at the Þeistareykir area. The interpolation method is algorithm GPSGridder implemented in Generic Mapping Tools (GMT). See the text for the explanation of parameters.

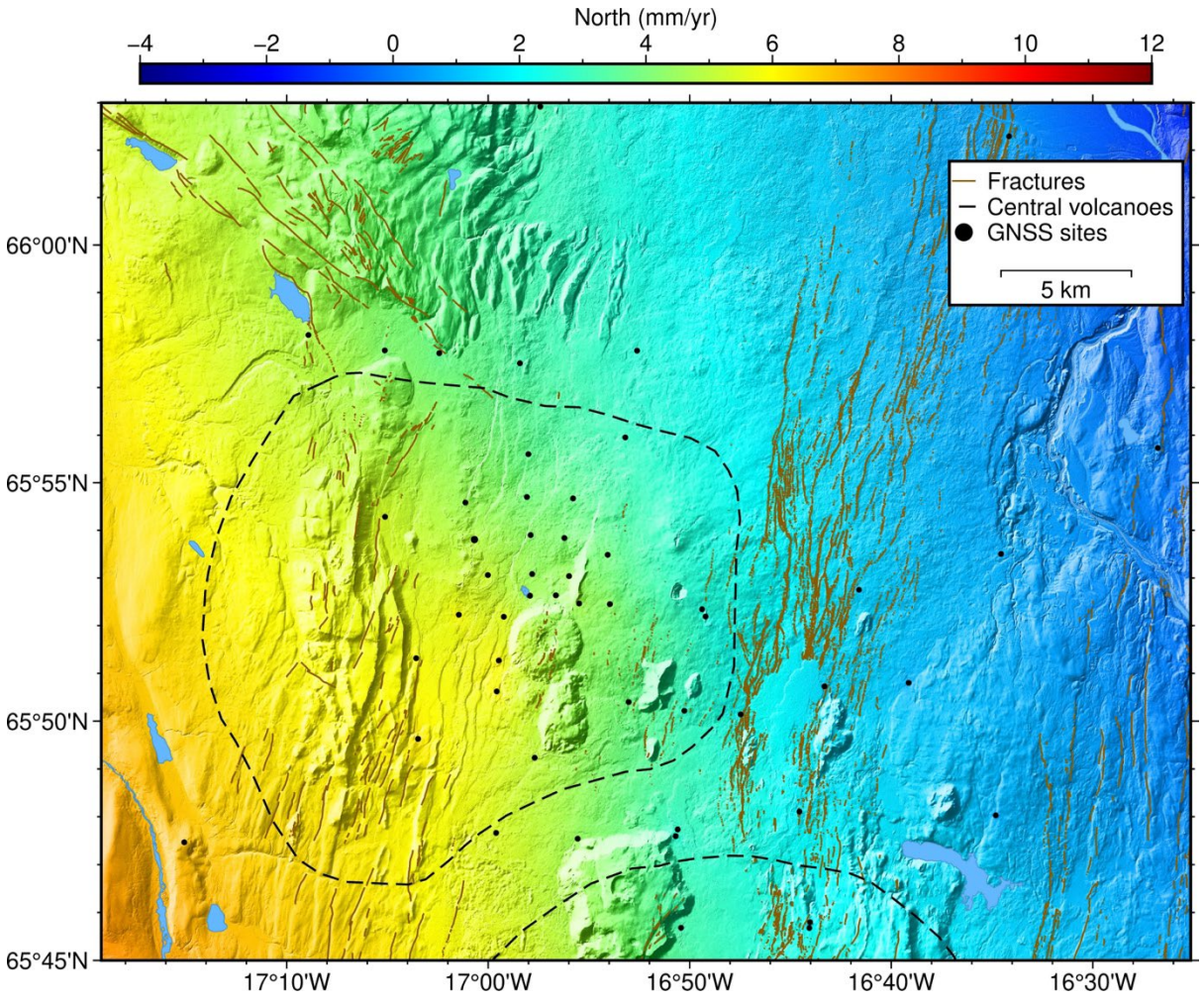

Figure 11. Interpolated GNSS north-component displacement velocity field at the Þeistareykir area. The interpolation method is algorithm GPSGridder implemented in Generic Mapping Tools (GMT). See the text for the explanation of parameters.

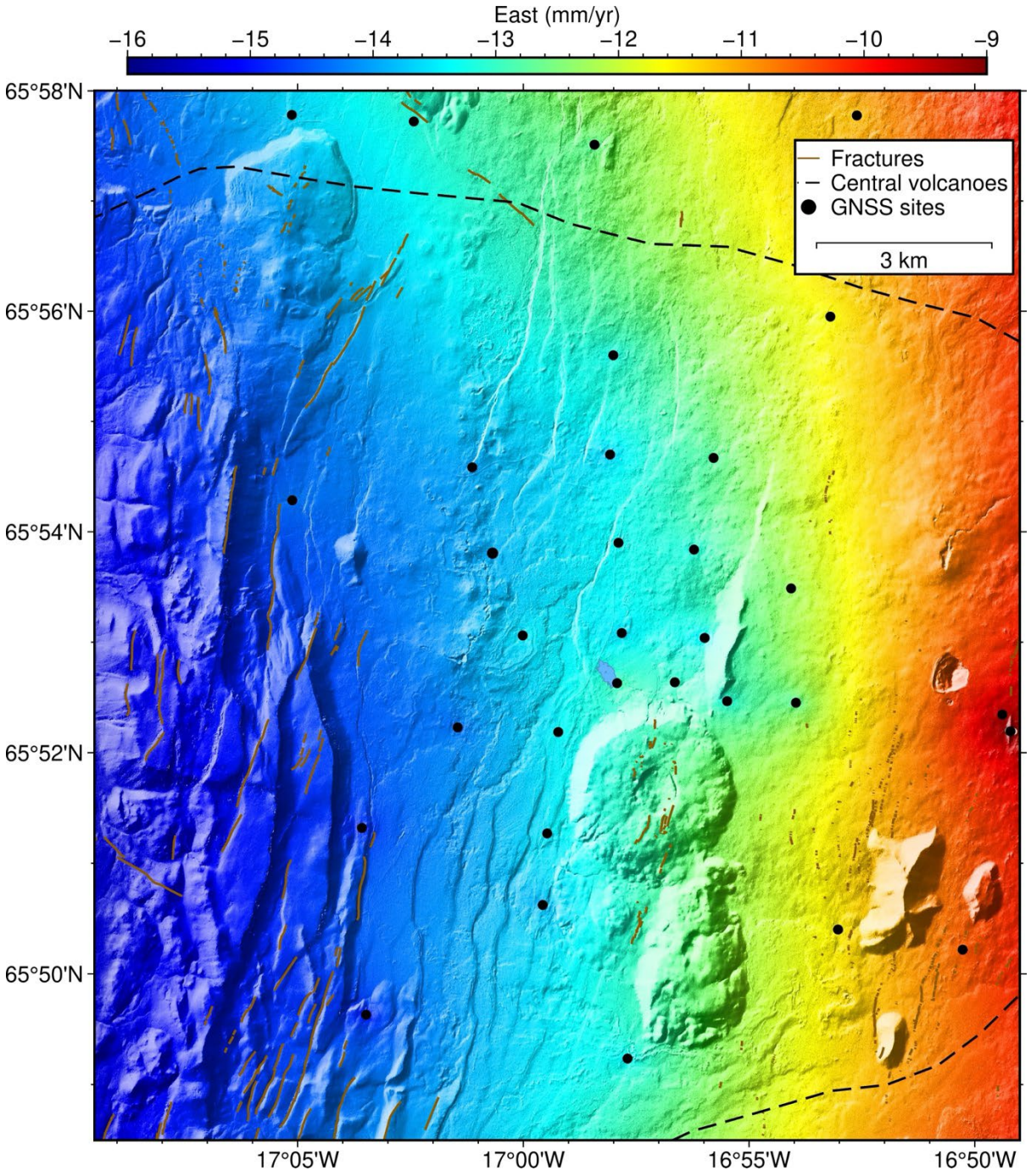

Figure 12. Interpolated GNSS east-component displacement velocity field in a smaller area of Þeistareykir. The interpolation method is algorithm GPSGridder implemented in Generic Mapping Tools (GMT). See the text for the explanation of parameters.

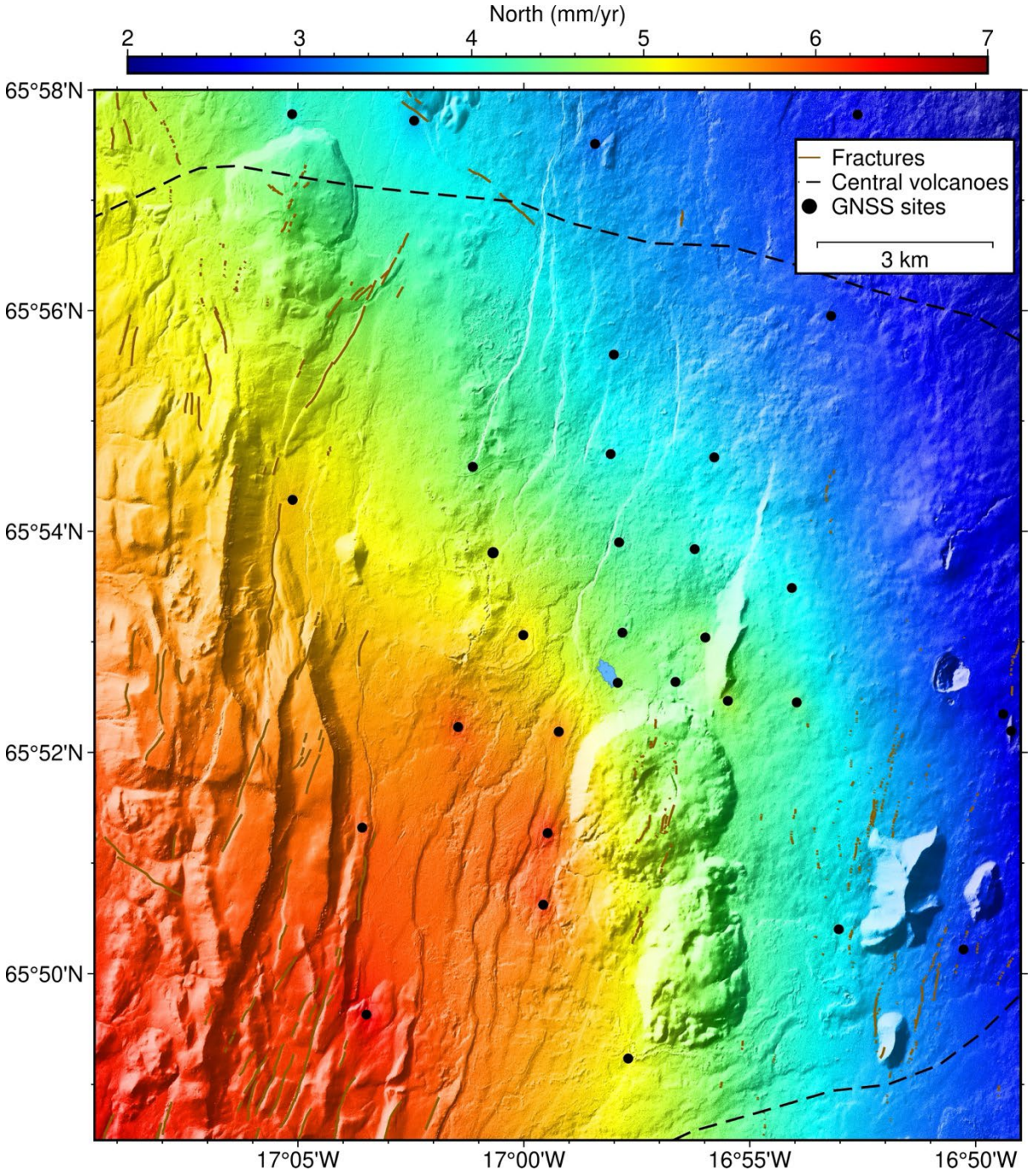

Figure 13. Interpolated GNSS north-component displacement velocity field in a smaller area of Þeistareykir. The interpolation method is algorithm GPSGridder implemented in Generic Mapping Tools (GMT). See the text for the explanation of parameters.

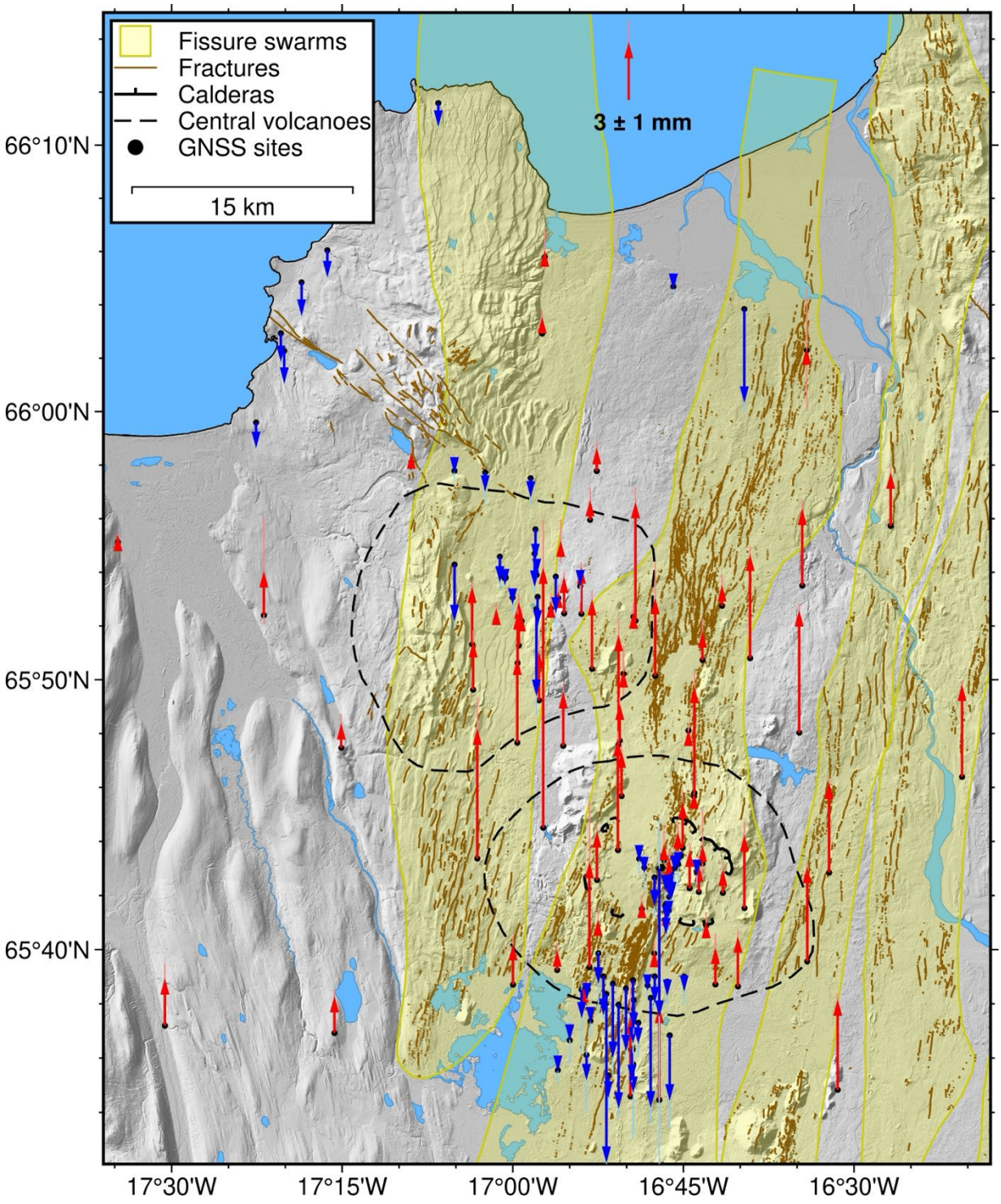

Figure 14. GNSS vertical displacement velocity field at the Þeistareykir and Krafla areas. The light blue and light red lines indicate the uncertainties of velocity estimates (standard deviation, ~68% confidence interval). The time span of GNSS time series deriving the velocity field is explained in the text.

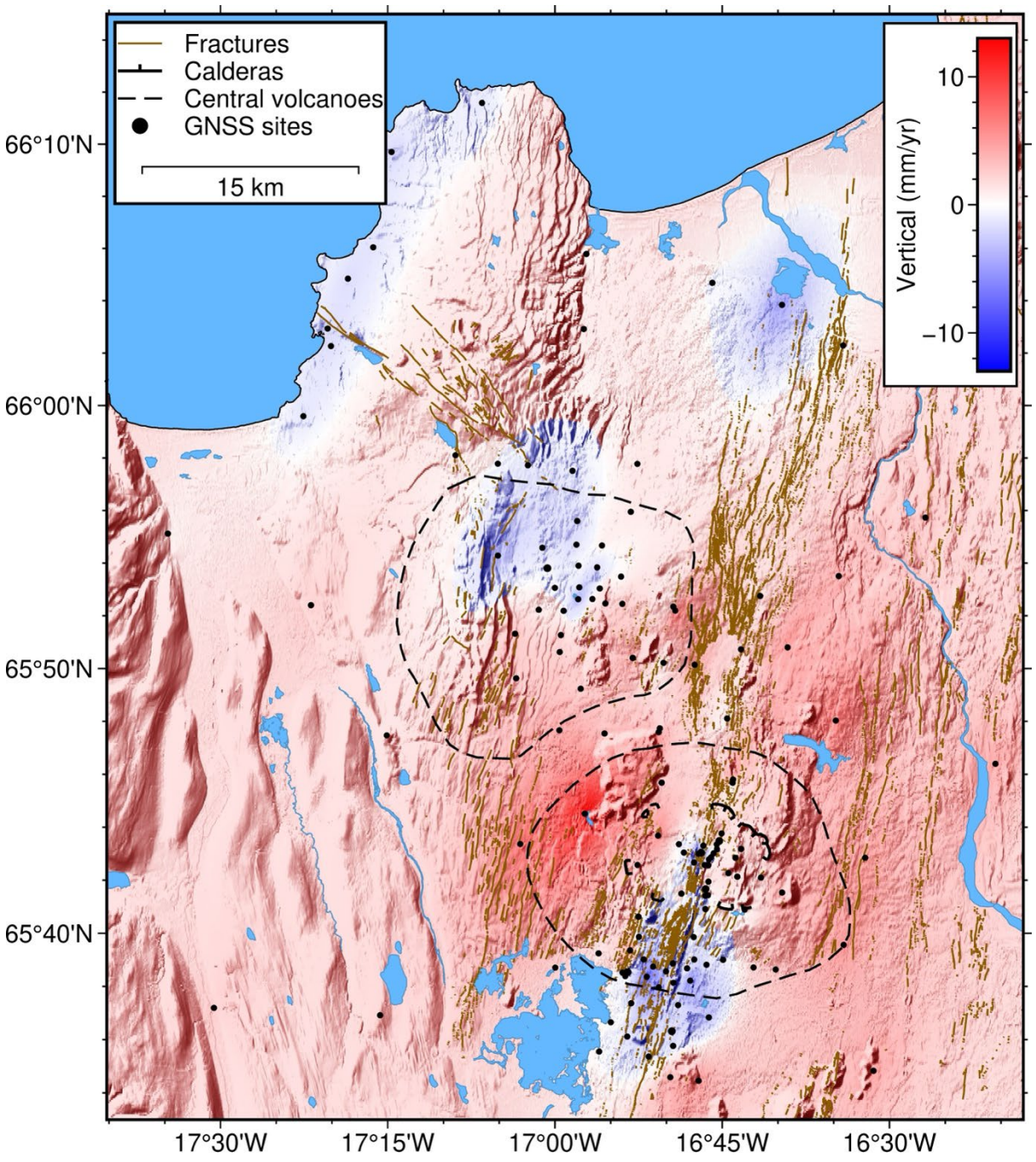

Figure 15. Interpolated GNSS up-component displacement velocity field at the Þeistareykir and Krafla areas. See the text for the explanation of the interpolation method.

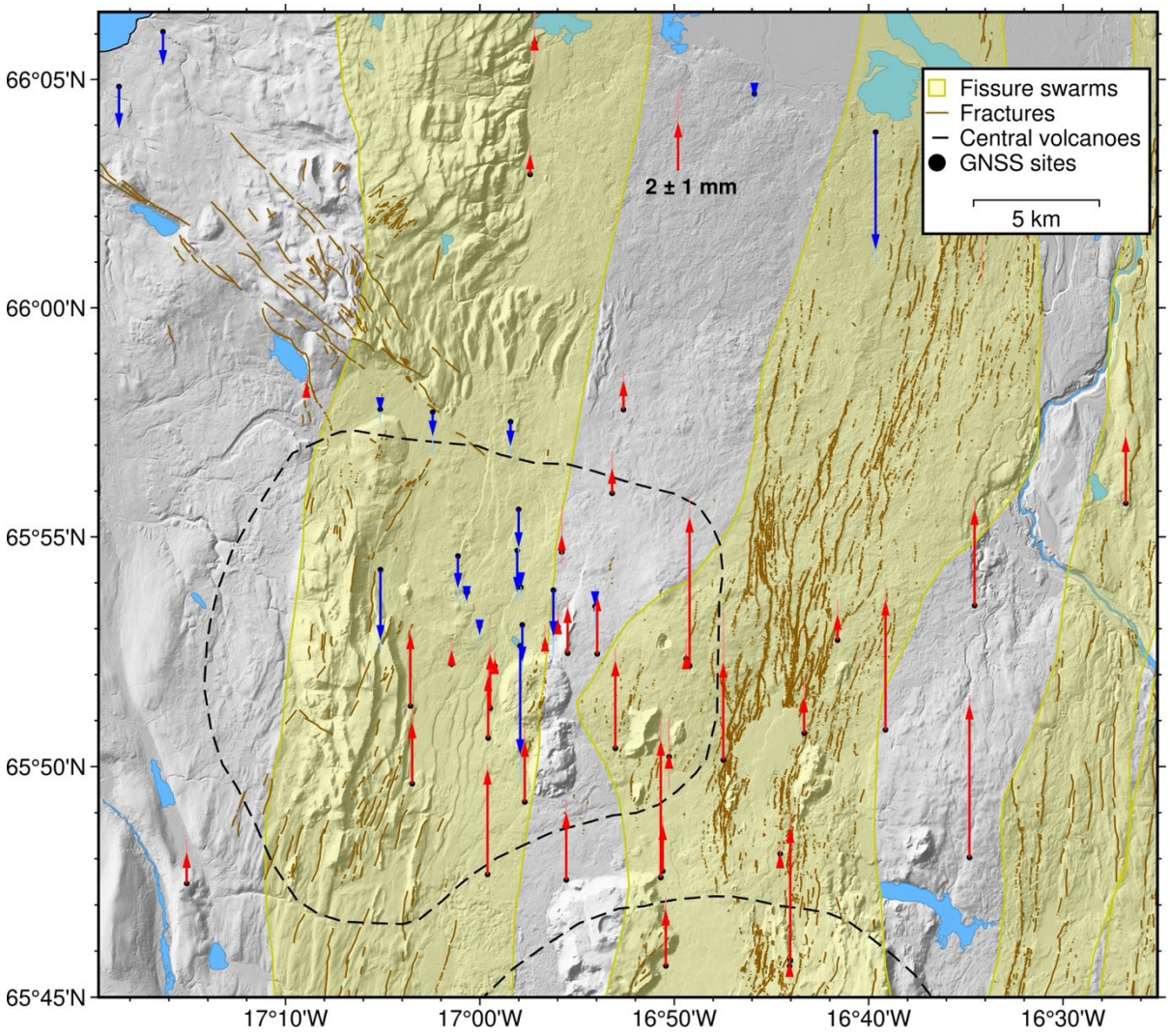

Figure 16. GNSS vertical displacement velocity field at the Þeistareykir area. The light blue and light red lines indicate the uncertainties of velocity estimates (standard deviation, ~68% confidence interval).

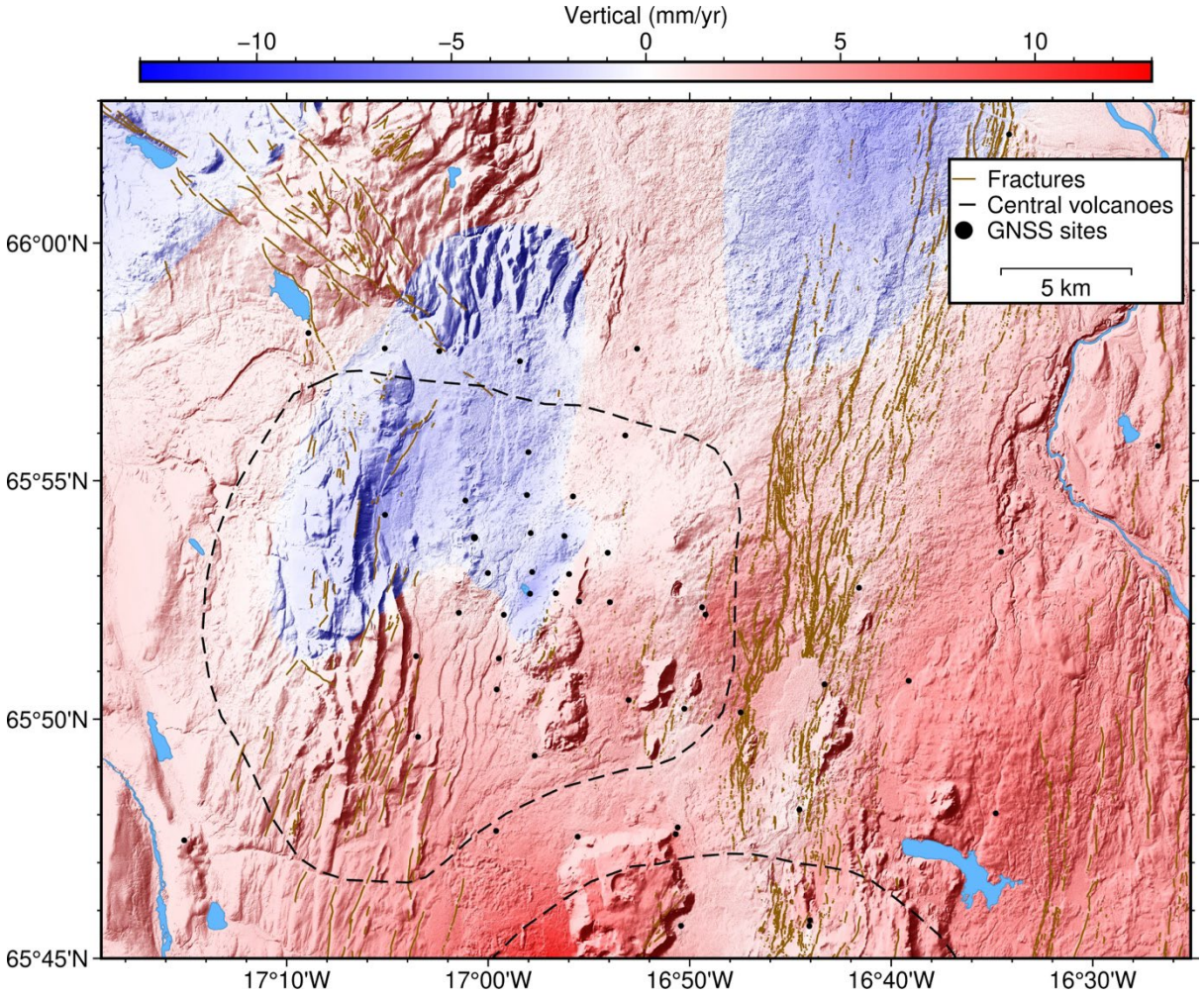

Figure 17. Interpolated GNSS up-component displacement velocity field at the Þeistareykir area. See the text for explanation of the interpolation method.

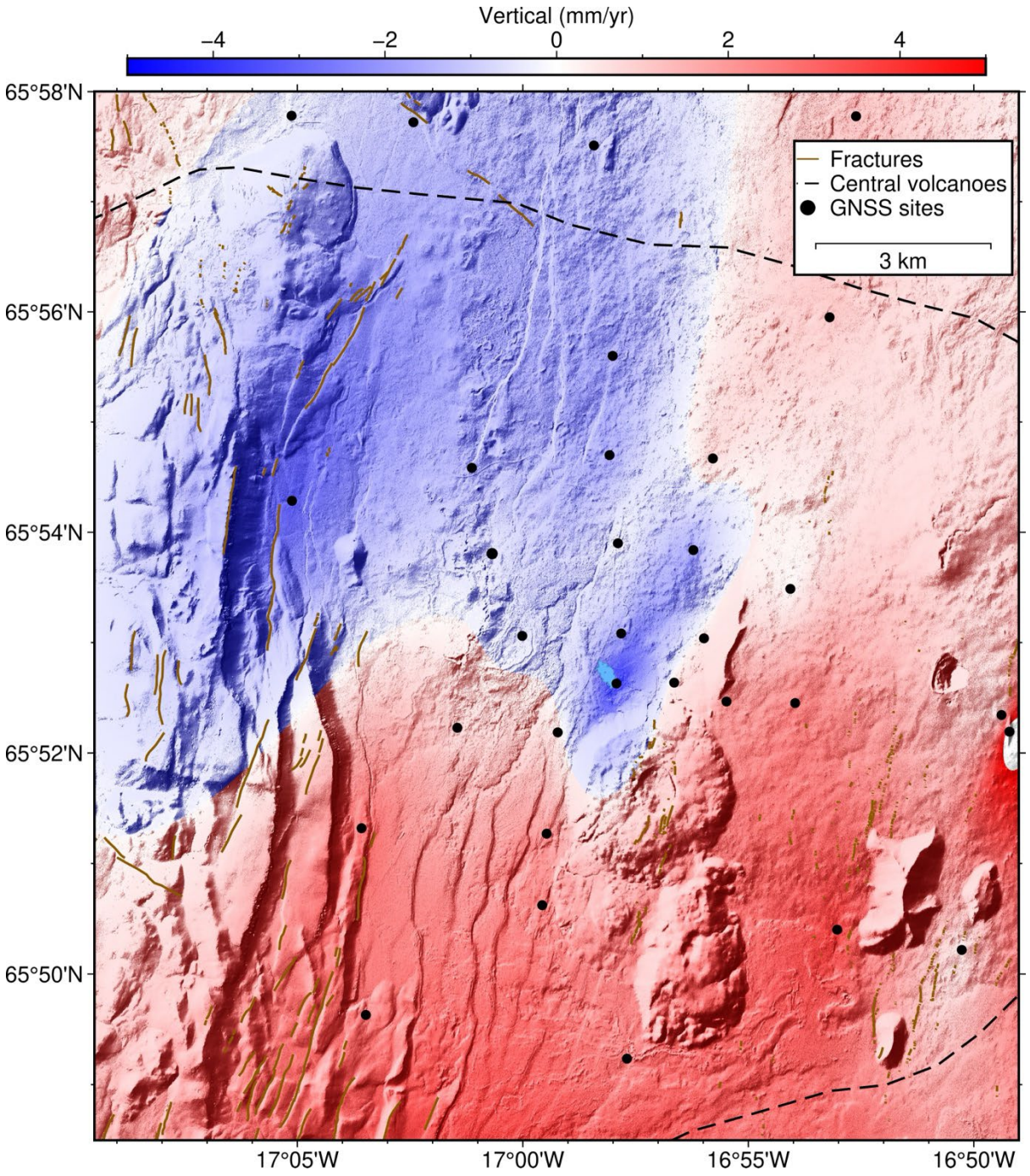

Figure 18. Interpolated GNSS up-component displacement velocity field at a smaller area of Þeistareykir. See the text for explanation of the interpolation method.

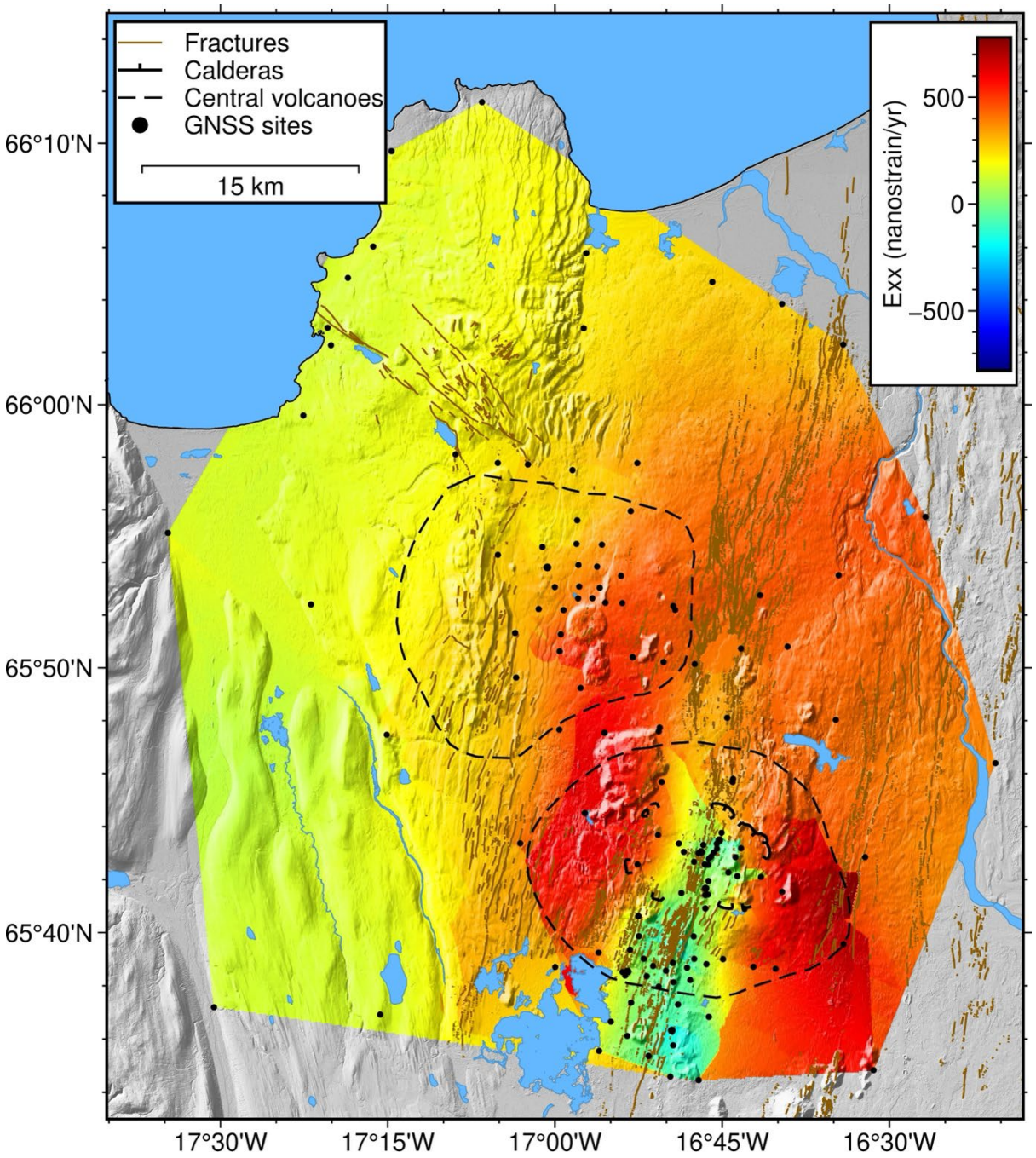

Figure 19. East-component strain rate at the Þeistareykir and Krafla areas derived by GNSS horizontal velocity field. The estimation is implemented with velocity interpolation for strain rate (VISR; Shen et al., 2015), where Gaussian decay function is applied for distance-dependent weighting and Voronoi cell areal weighting function is applied for Spatially dependent weighting. Spatial smoothing constants are set between 1 and 100 km with an interval of 1 km. The net weighting threshold (output smoothness) is 20.

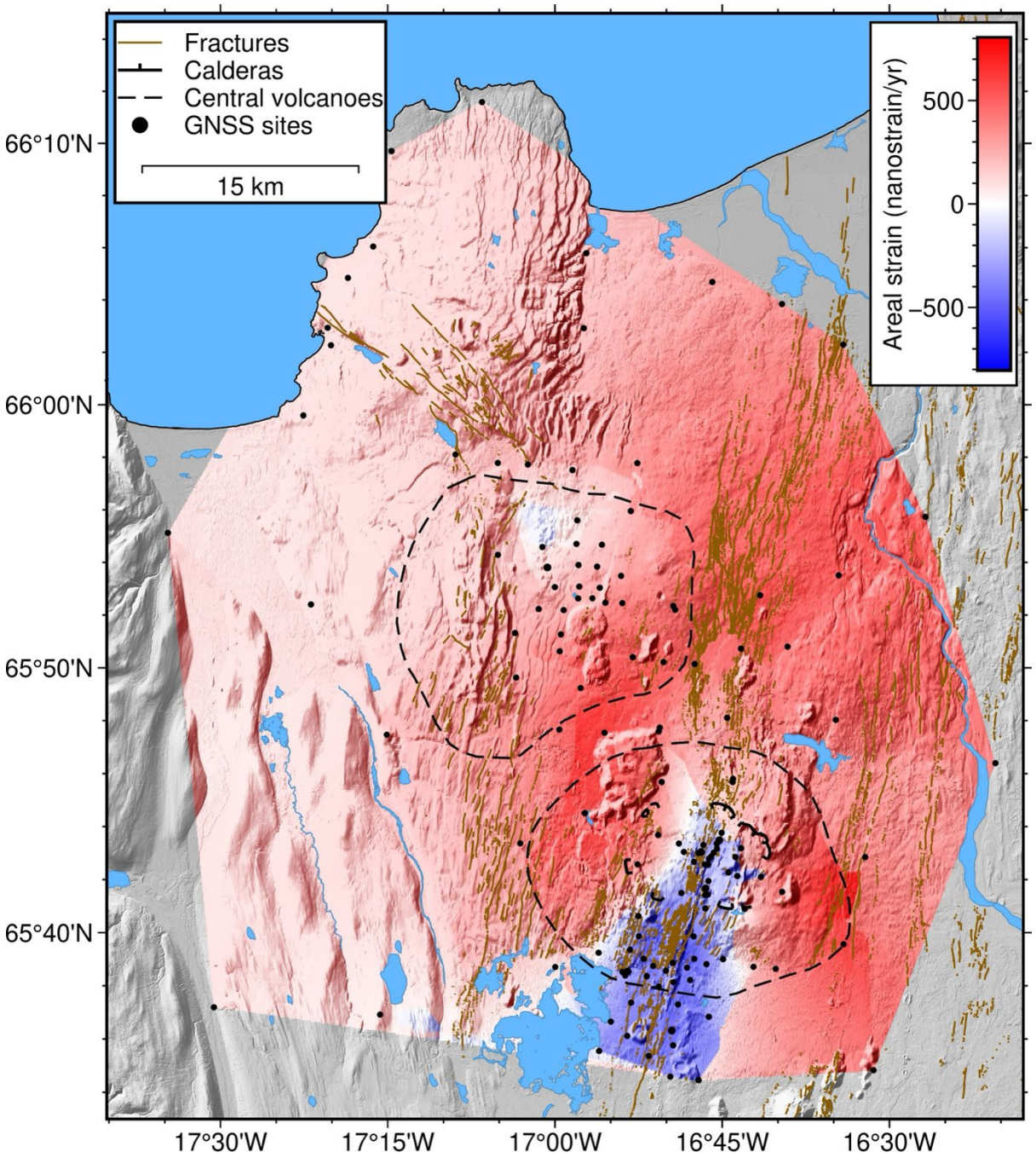

Figure 20. 2D areal strain rate at the Þeistareykir and Krafla areas derived by GNSS horizontal velocity field. The estimation is implemented with velocity interpolation for strain rate (VISR; Shen et al., 2015), where Gaussian decay function is applied for distance-dependent weighting and Voronoi cell areal weighting function is applied for Spatially dependent weighting. Spatial smoothing constants are set between 1 and 100 km with an interval of 1 km. The net weighting threshold (output smoothness) is 20.

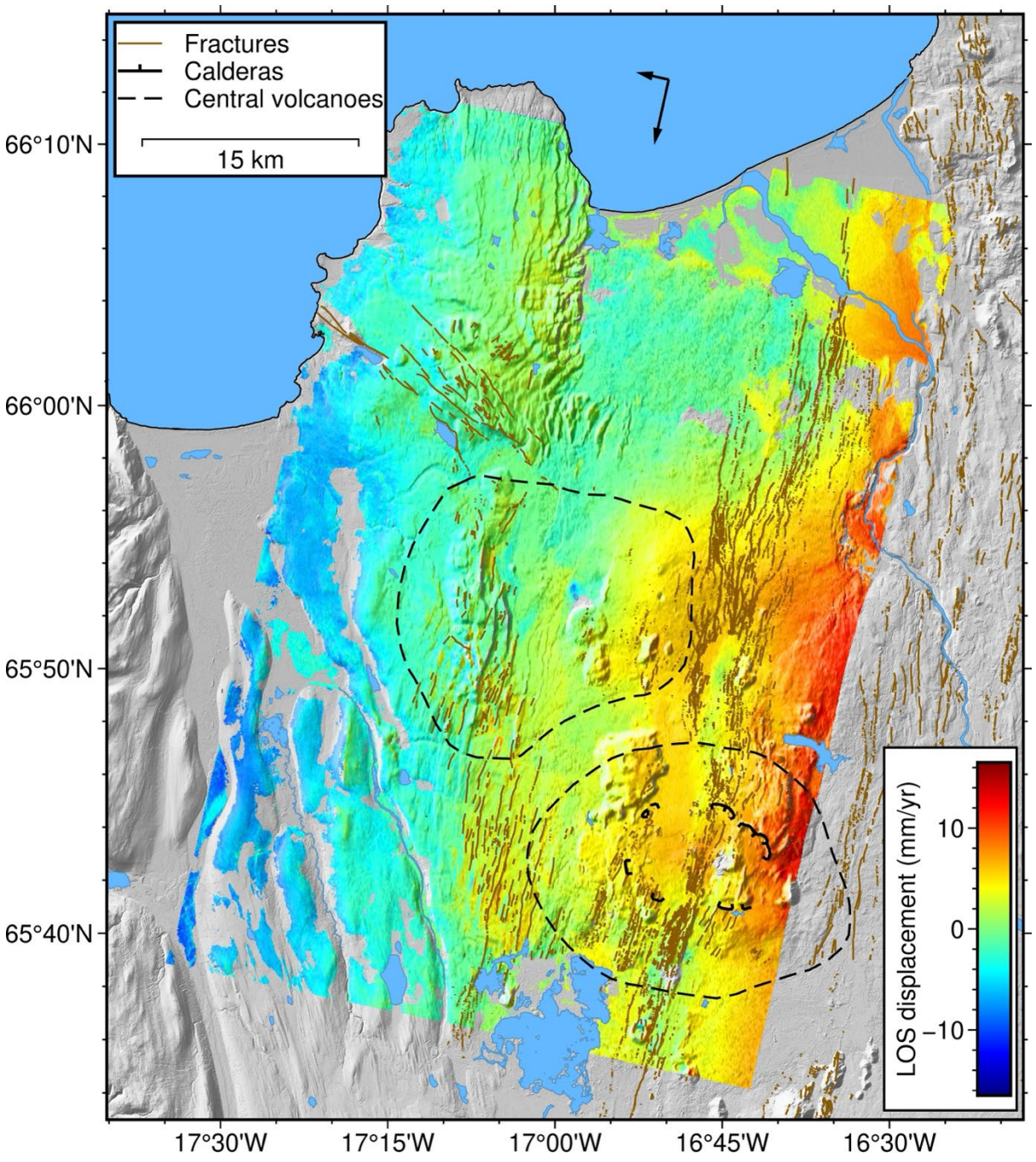

Figure 21. Inferred rate of yearly averaged line-of-sight displacement (LOS velocity) inferred from Sentinel-1 Track T9 (descending) in 2017–2022. The azimuth direction of the satellite is 192.5° to the north, and the incidence angle is 36.6°.

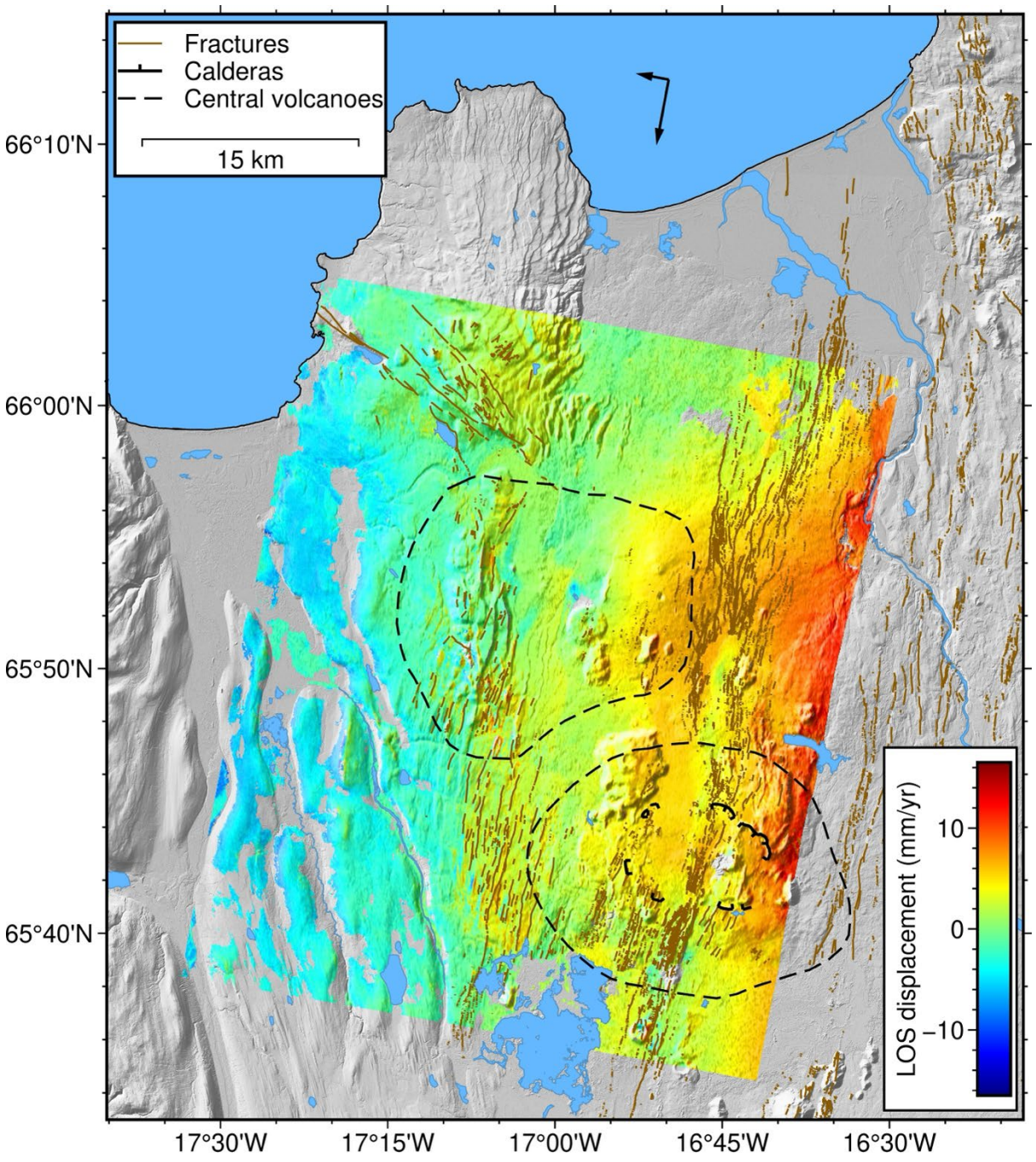

Figure 22. Inferred rate of yearly averaged line-of-sight displacement (LOS velocity) inferred from Sentinel-1 Track T111 (descending) in 2017–2022. The azimuth direction of the satellite is 190.6° to the north, and the incidence angle is 42°.

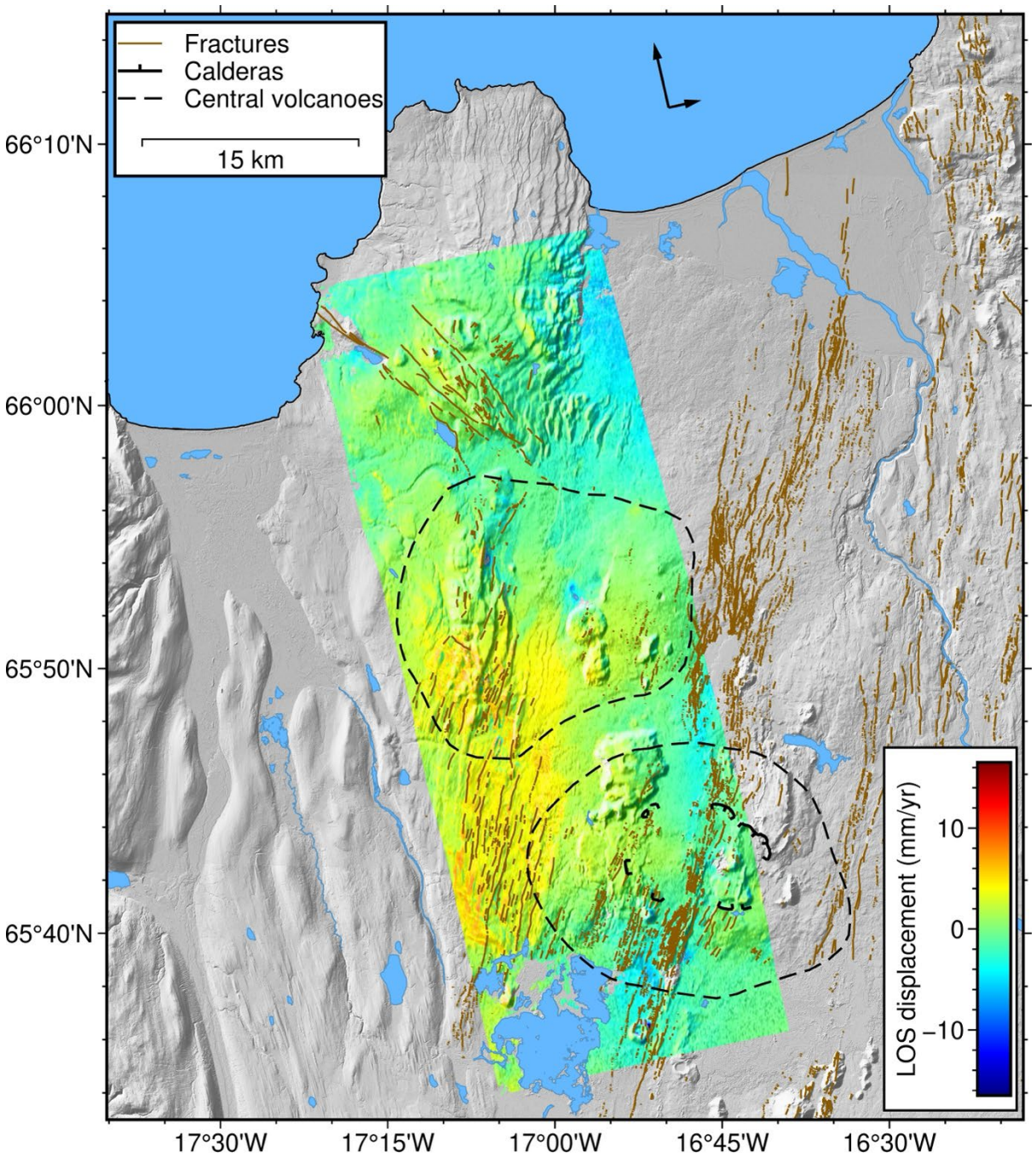

Figure 23. Inferred rate of yearly averaged line-of-sight displacement (LOS velocity) inferred from Sentinel-1 Track T147 (descending) in 2017–2022. The azimuth direction of the satellite is 347.2° to the north, and the incidence angle is 35.5°.

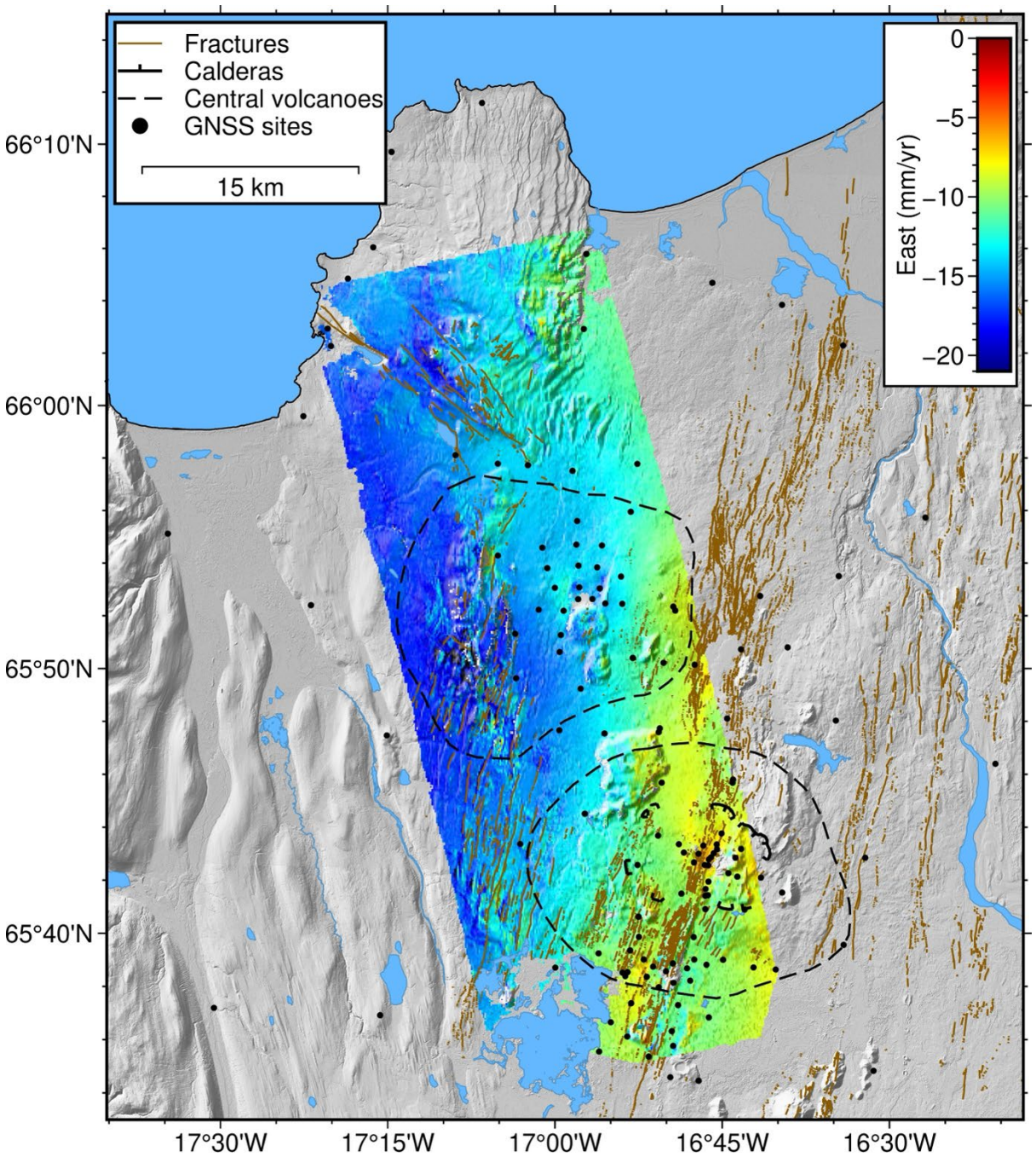

Figure 24. East-component displacement velocity field in the Þeistareykir and Krafla areas combining GNSS and InSAR observations with the SISTEM software. The InSAR displacements are derived from T9 and T147 (Figure 21 and Figure 23).

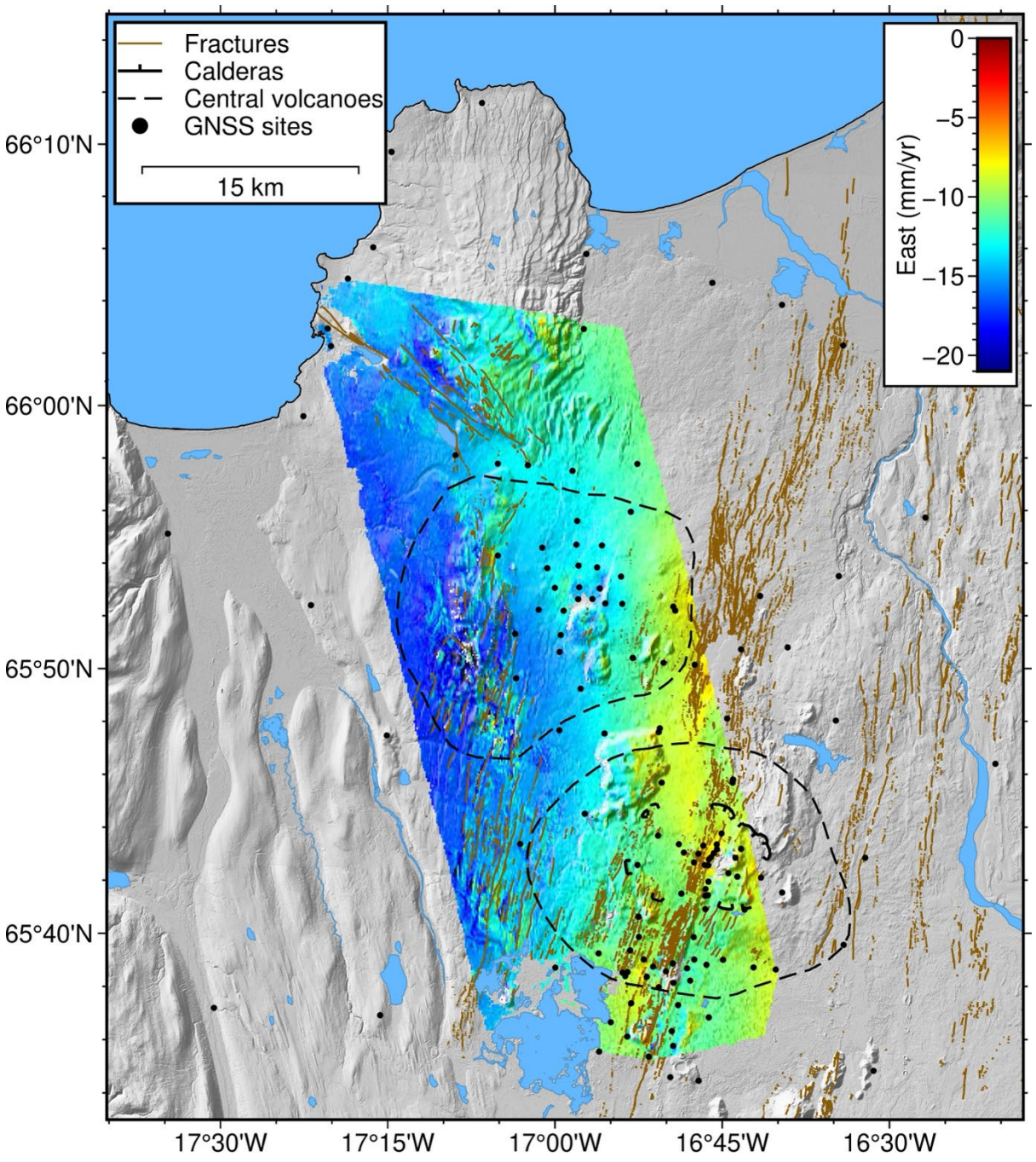

Figure 25. East-component displacement velocity field in the Þeistareykir and Krafla areas combining GNSS and InSAR observations with the SISTEM software. The InSAR displacements are derived from T111 and T147 (Figure 22 and Figure 23).

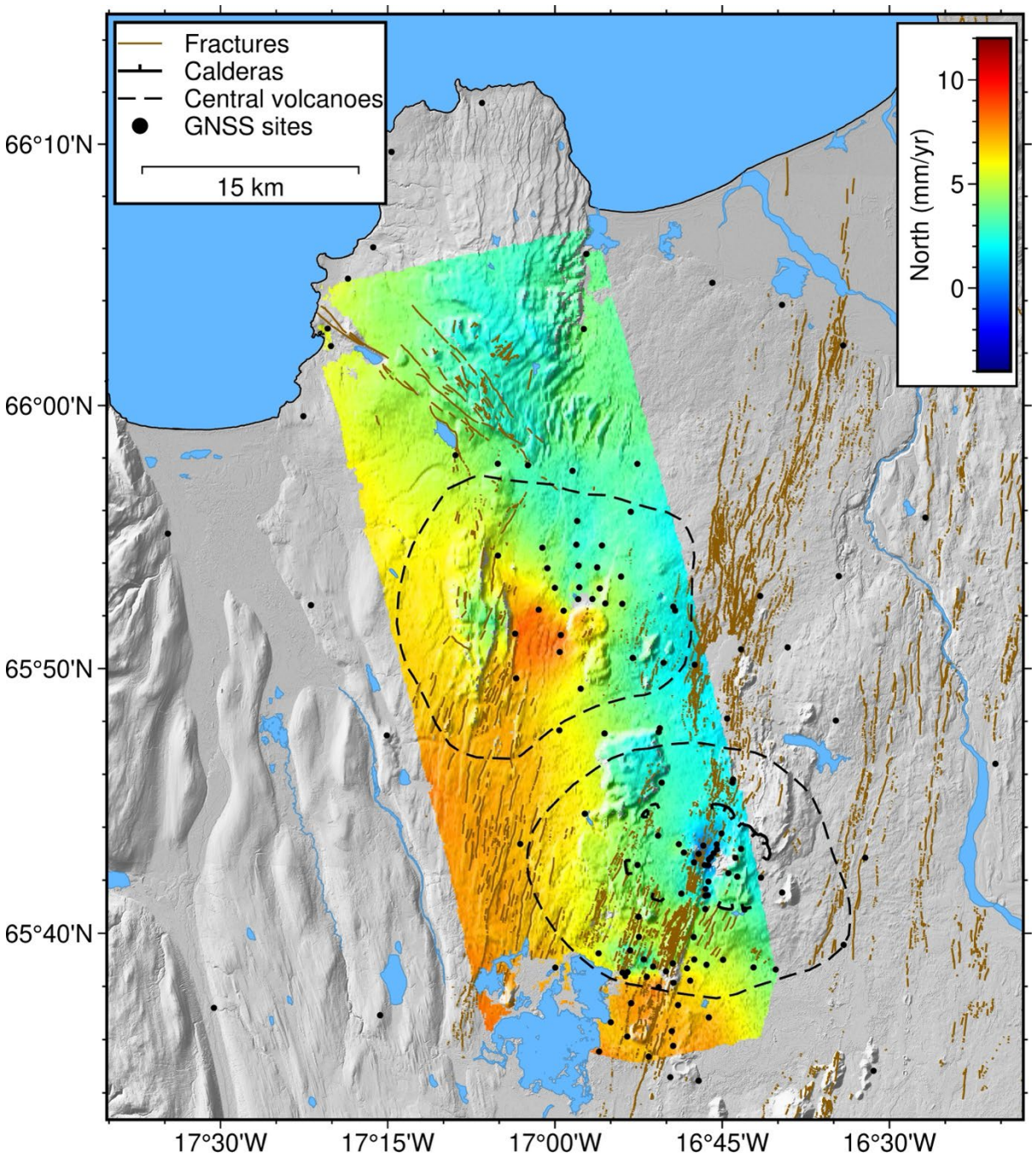

Figure 26. North-component displacement velocity field in the Þeistareykir and Krafla areas combining GNSS and InSAR observations with the SISTEM software. The InSAR displacements is derived from T9 and T147 (Figure 21 and Figure 23).

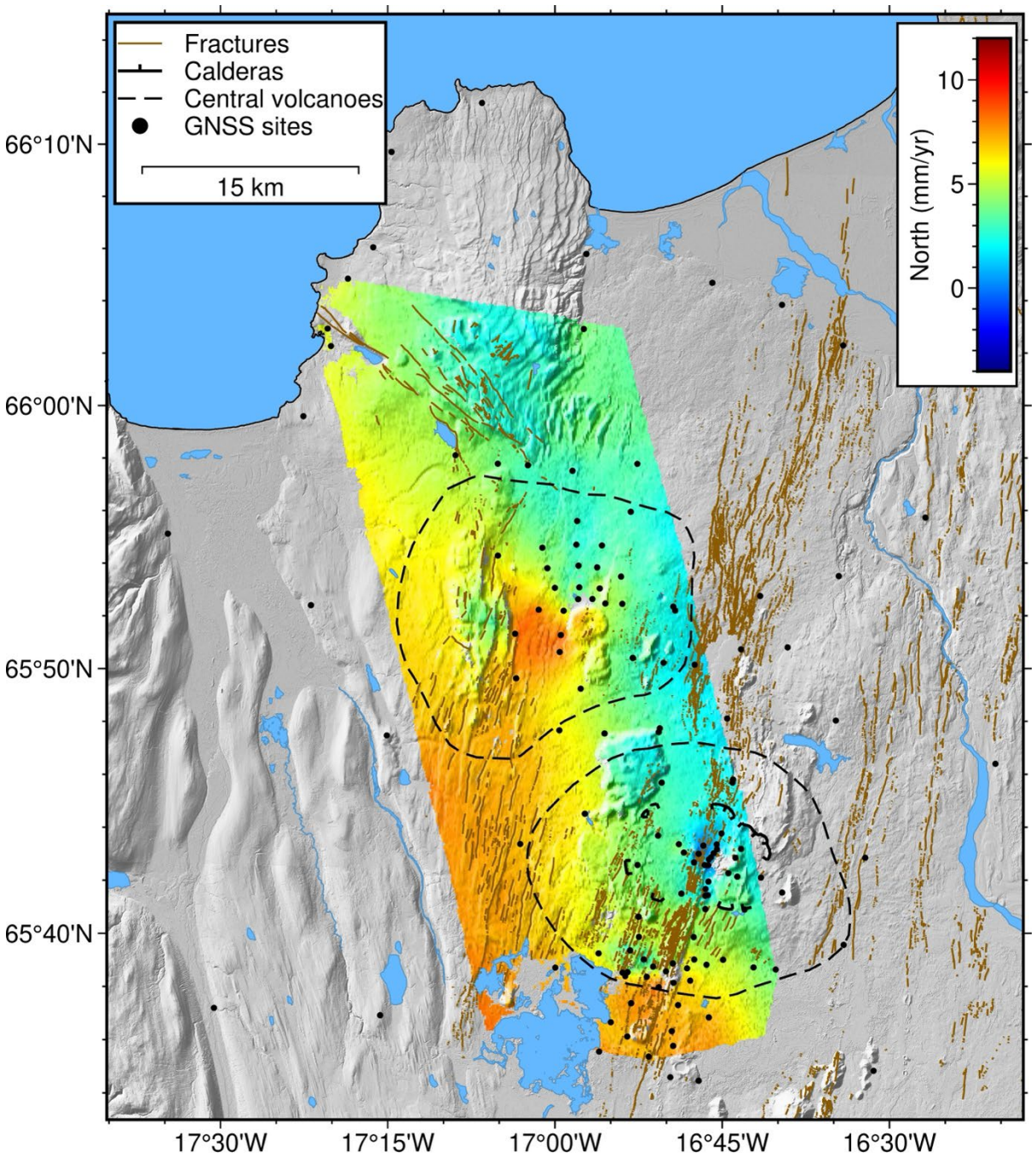

Figure 27. North-component displacement velocity field in the Þeistareykir and Krafla areas combining GNSS and InSAR observations with the SISTEM software. The InSAR displacements is derived from T111 and T147 (Figure 22 and Figure 23).

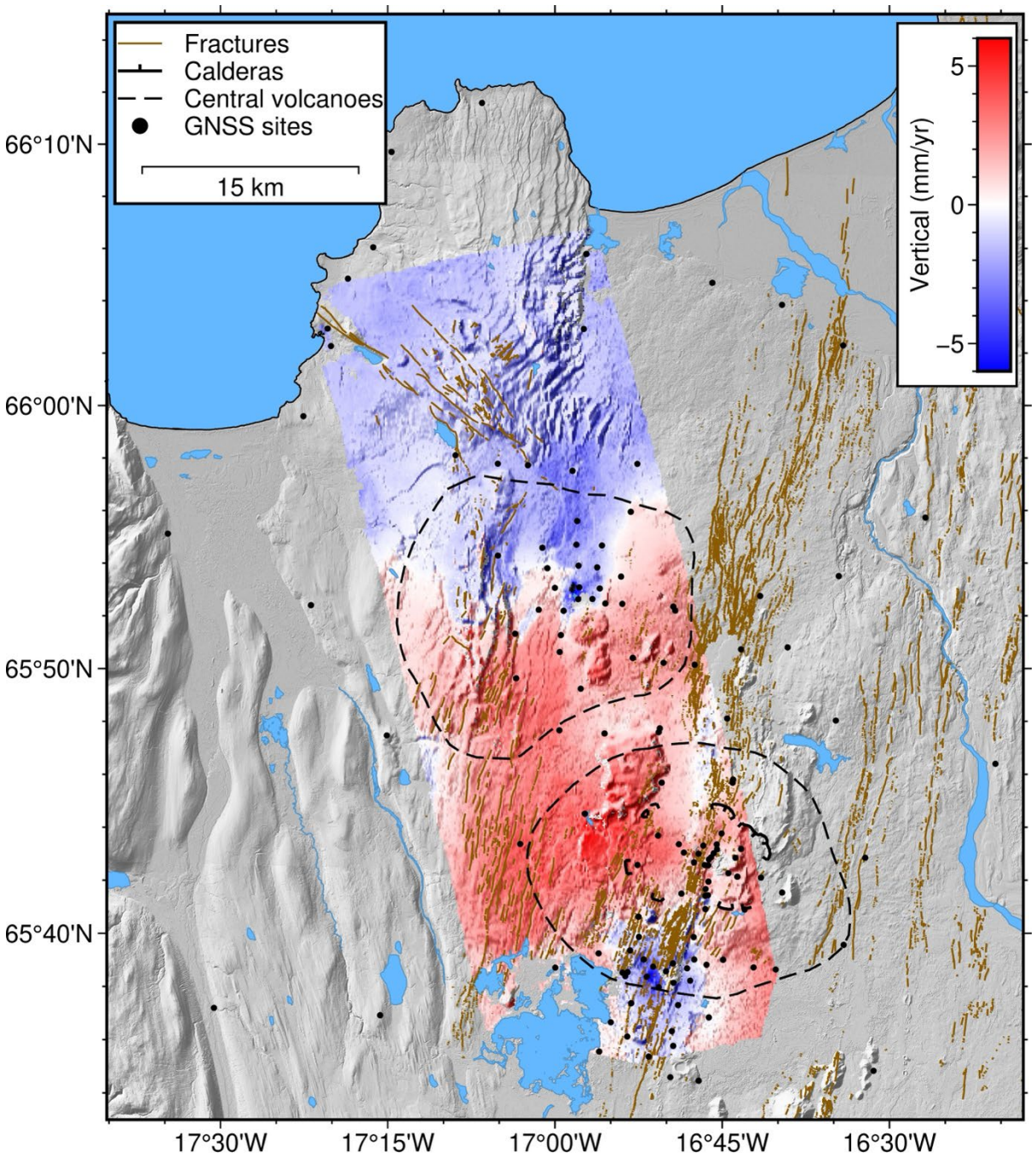

Figure 28. Vertical displacement velocity field in the Þeistareykir and Krafla areas combining GNSS and InSAR observations with the SISTEM software. The InSAR displacements is derived from T9 and T147 (Figure 21 and Figure 23).

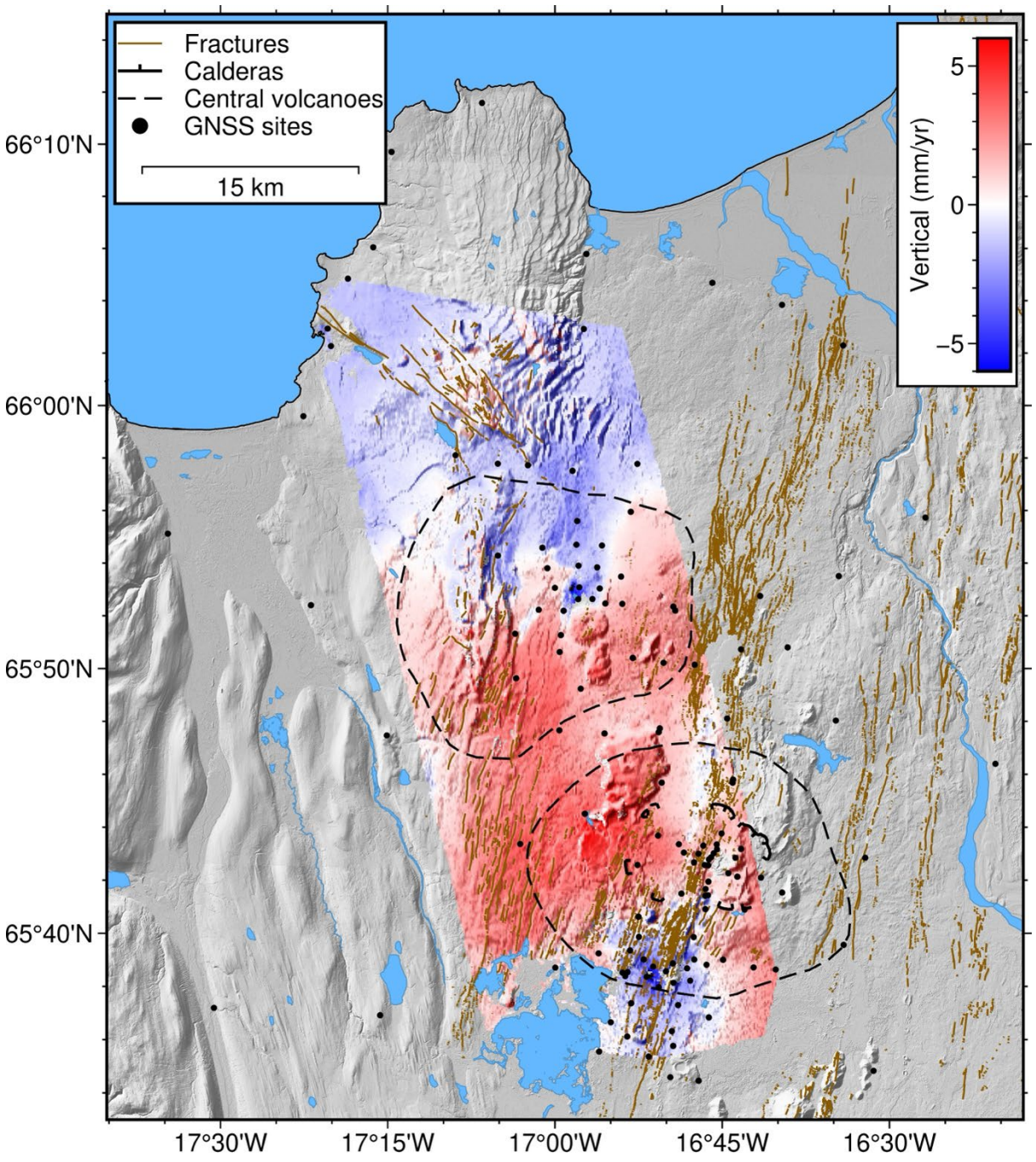

Figure 29. Vertical displacement velocity field in the Þeistareykir and Krafla areas combining GNSS and InSAR observations with the SISTEM software. The InSAR displacements is derived from T111 and T147 (Figure 22 and Figure 23).

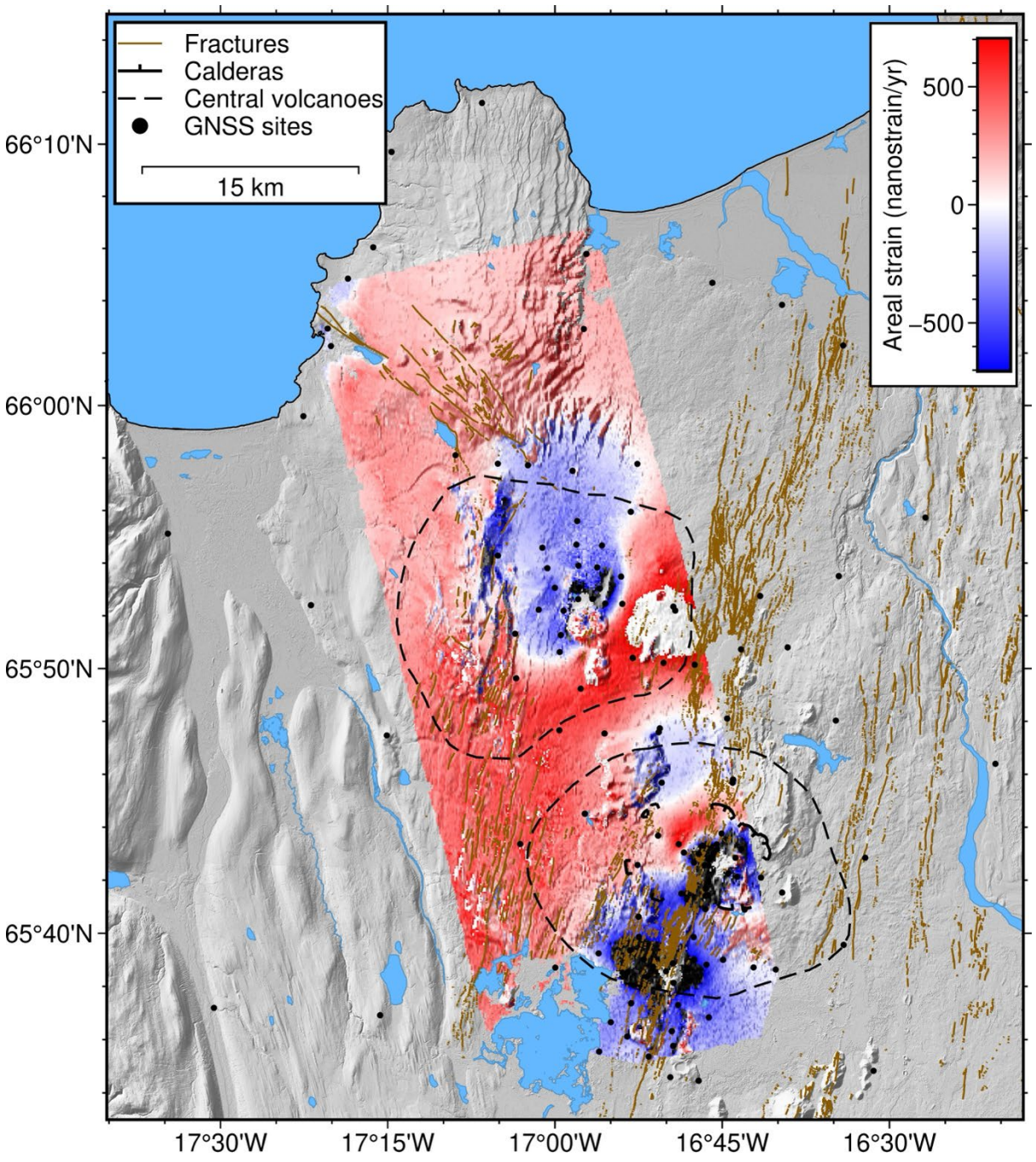

Figure 30. 2D areal strain rate in the Þeistareykir and Krafla areas combining GNSS and InSAR observations with the SISTEM software. The InSAR displacements is derived from T9 and T147 (Figure 21 and Figure 23).

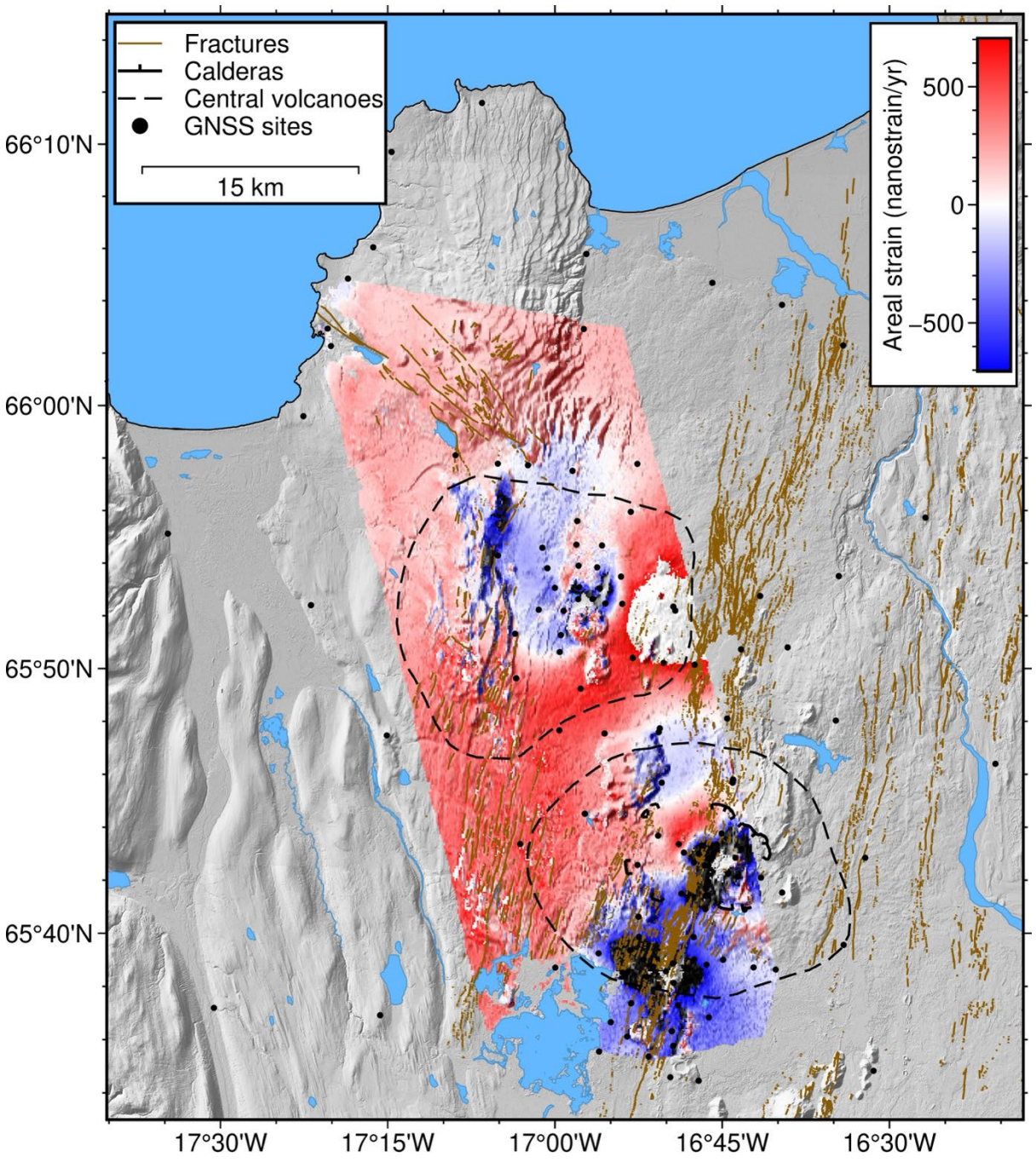

Figure 31. 2D areal strain rate in the Þeistareykir and Krafla areas combining GNSS and InSAR observations with the SISTEM software. The InSAR displacements is derived from T111 and T147 (Figure 22 and Figure 23).

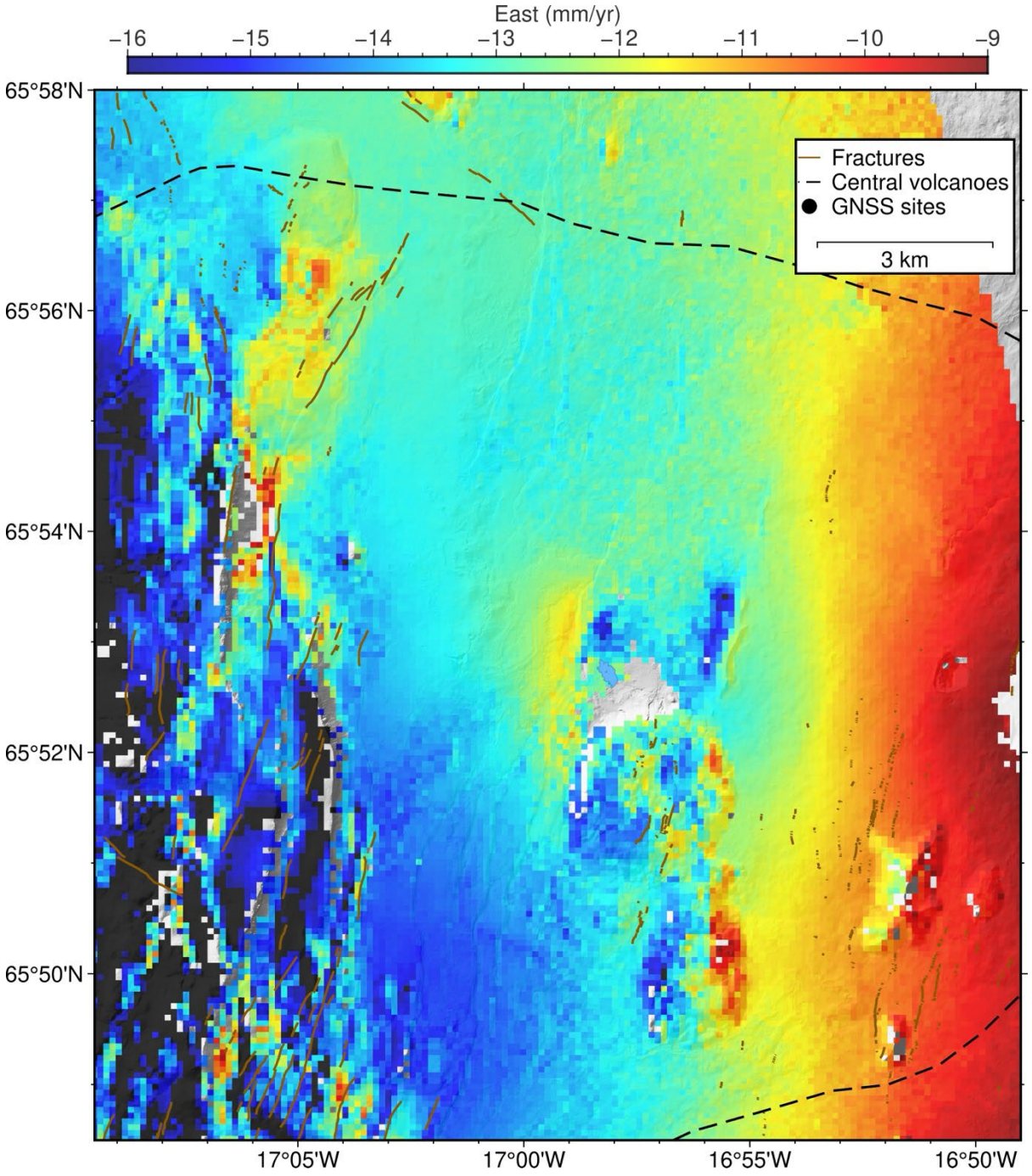

Figure 32. East-component displacement velocity field at a smaller area of Þeistareykir combining GNSS and InSAR observations with the SISTEM software. The InSAR displacements is derived from T9 and T147 (Figure 21 and Figure 23).

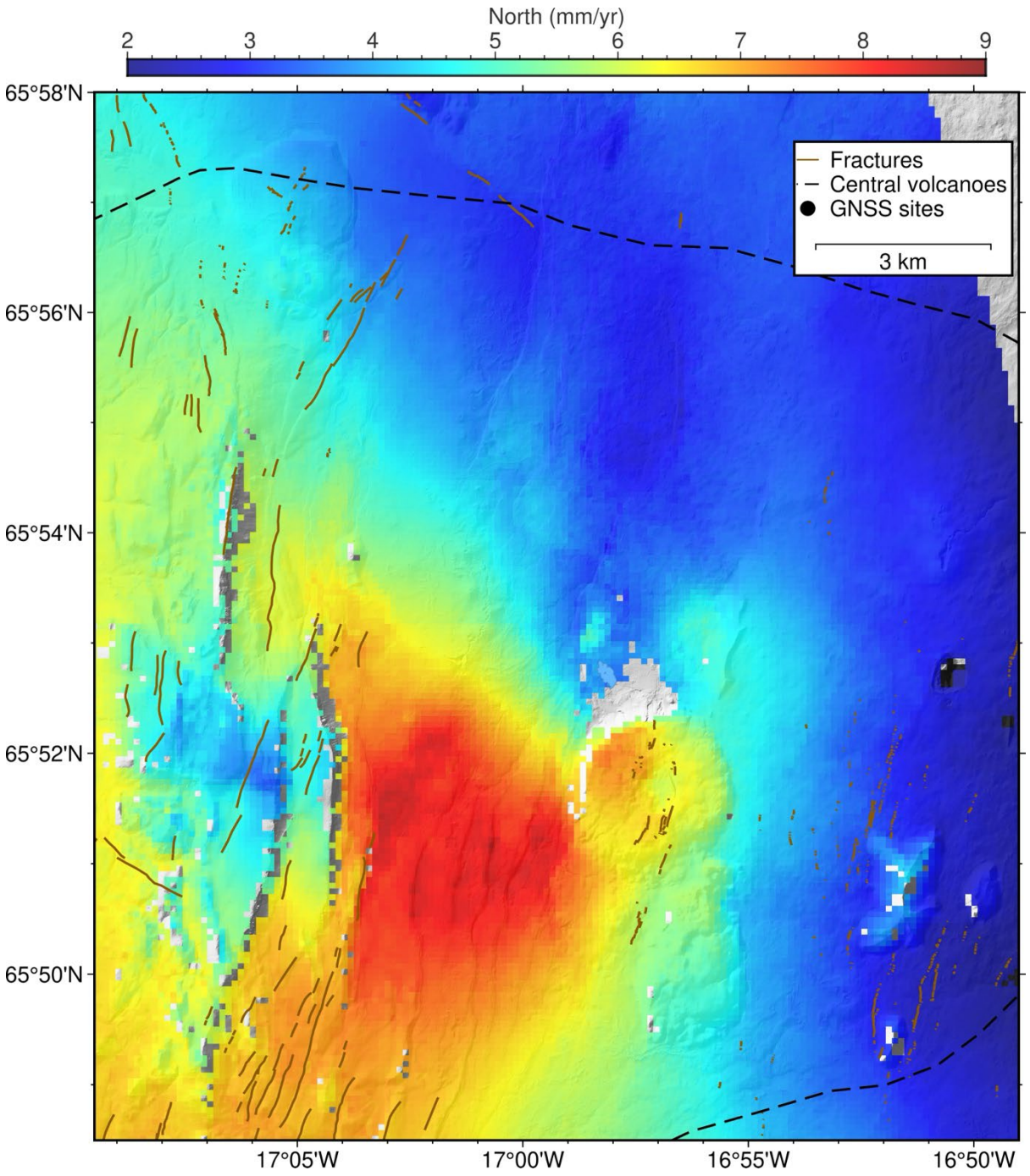

Figure 33. North component displacement velocity field at a smaller area of Þeistareykir combining GNSS and InSAR observations with the SISTEM software. The InSAR displacements is derived from T9 and T147 (Figure 21 and Figure 23).

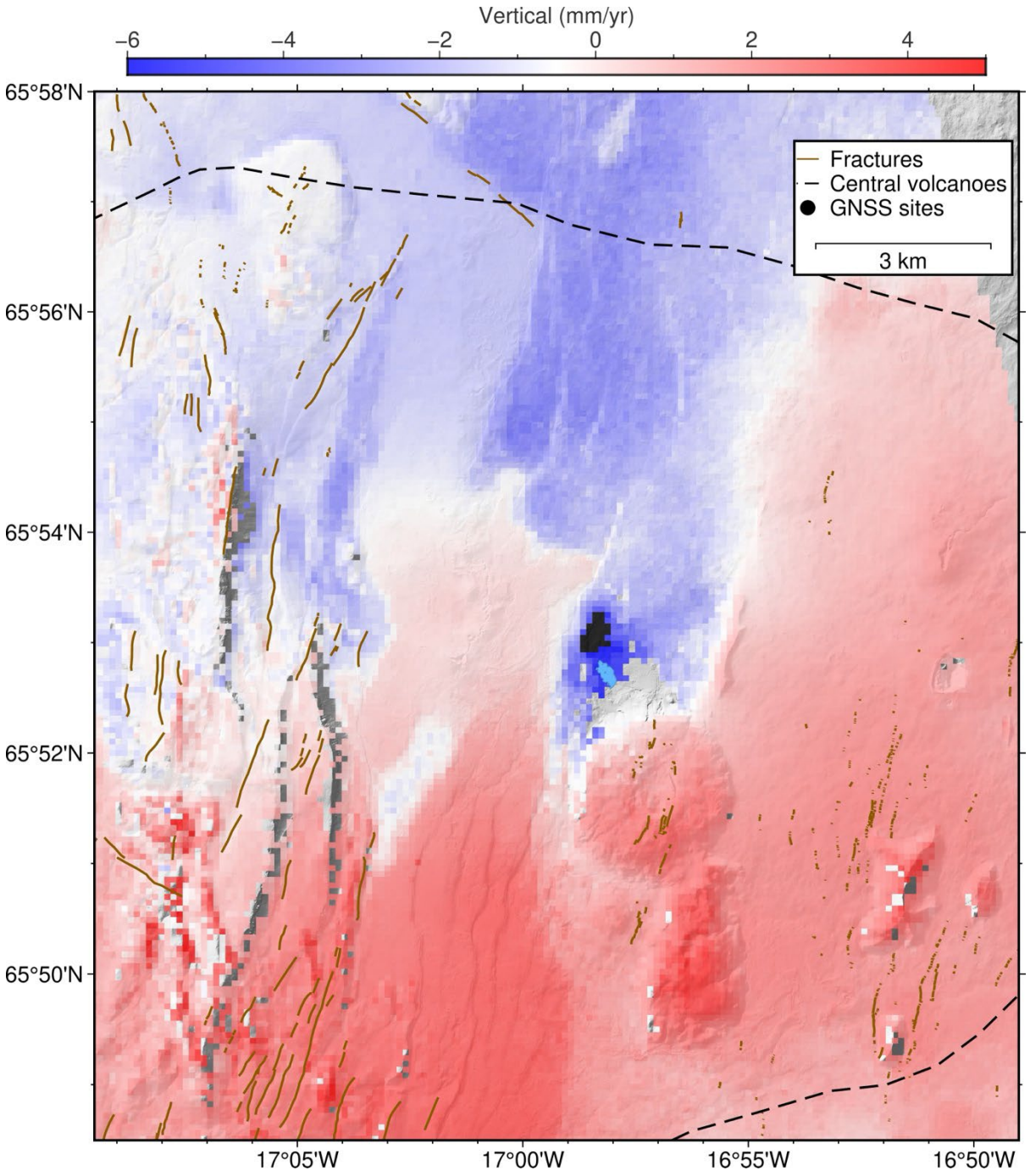

Figure 34. Vertical displacement velocity field at a smaller area of Þeistareykir combining GNSS and InSAR observations with the SISTEM software. The InSAR displacements is derived from T9 and T147 (Figure 21 and Figure 23).

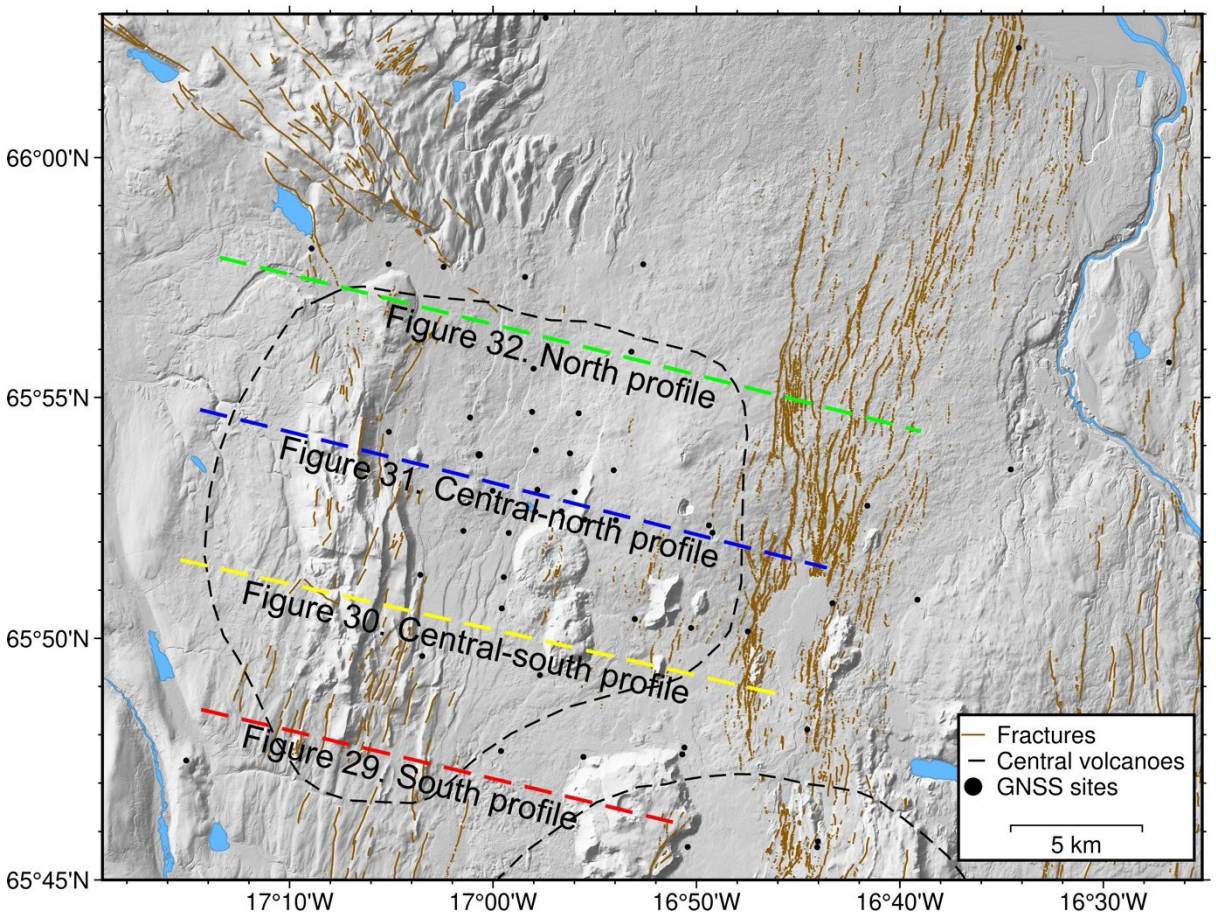

Figure 35. Map showing four profiles used to evaluate long-term displacements in the Þeistareykir area.

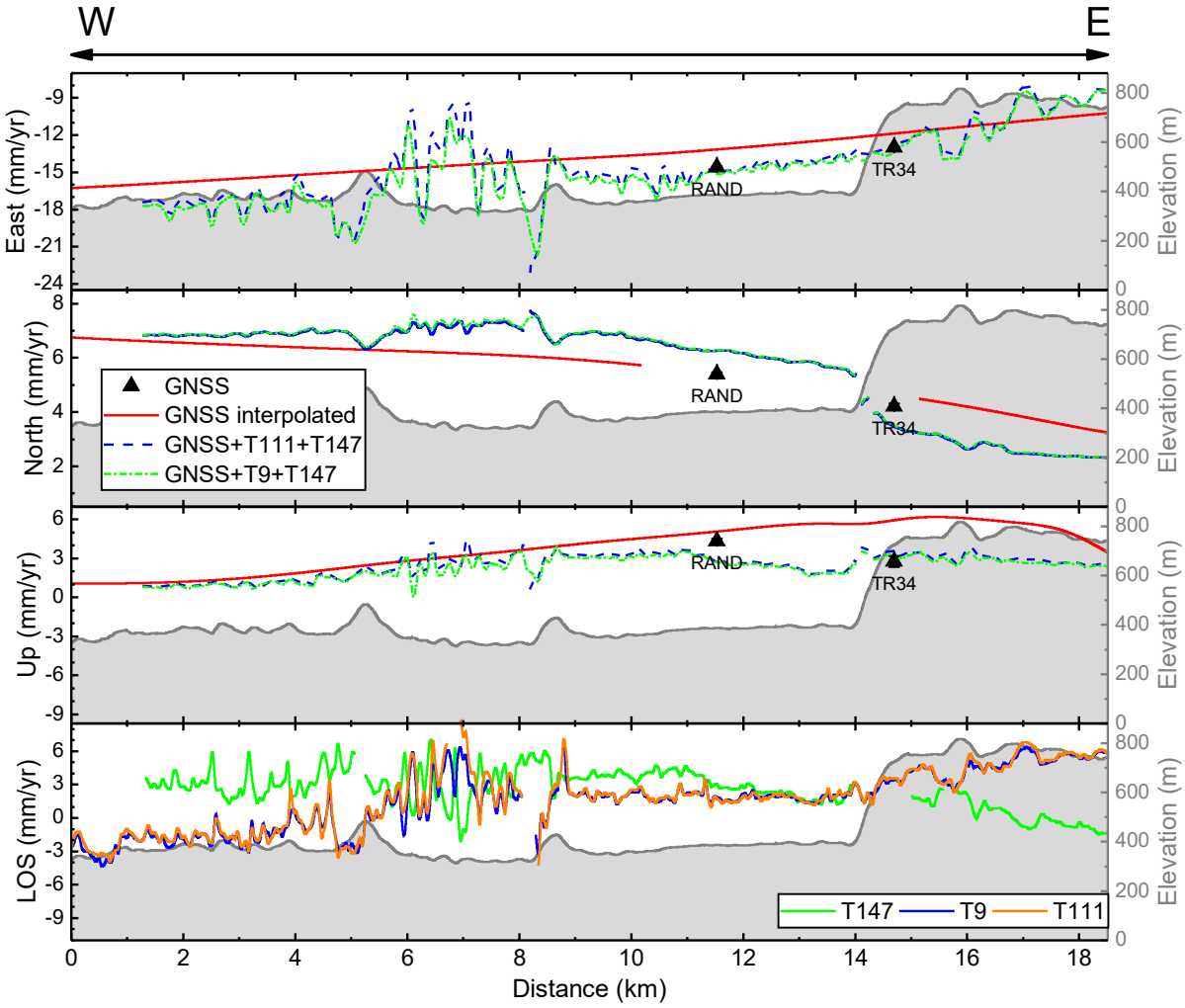

Figure 36. South profile of long-term displacement in the Þeistareykir area. The triangles show the displacement velocities at near-by GNSS sites projected onto the profile at the same longitude. GNSS interpolated, GNSS+T111+T147, and GNSS+T9+T147 are profiles extracted from corresponding maps.

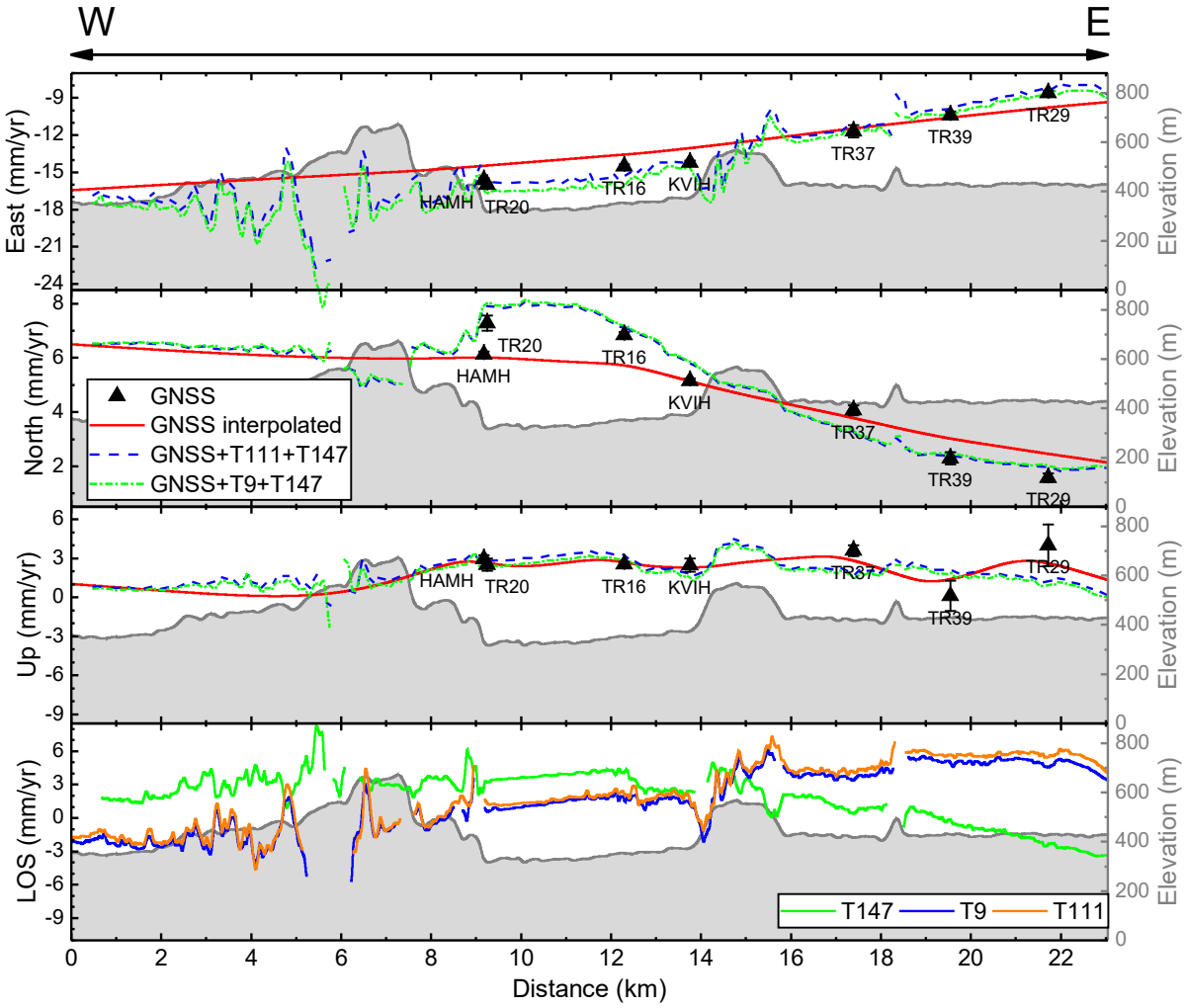

Figure 37. Central-south profile of long-term displacement in the Þeistareykir area. The triangles show the displacement velocities at near-by GNSS sites projected onto the profile at the same longitude. GNSS interpolated, GNSS+T111+T147, and GNSS+T9+T147 are profiles extracted from corresponding maps.

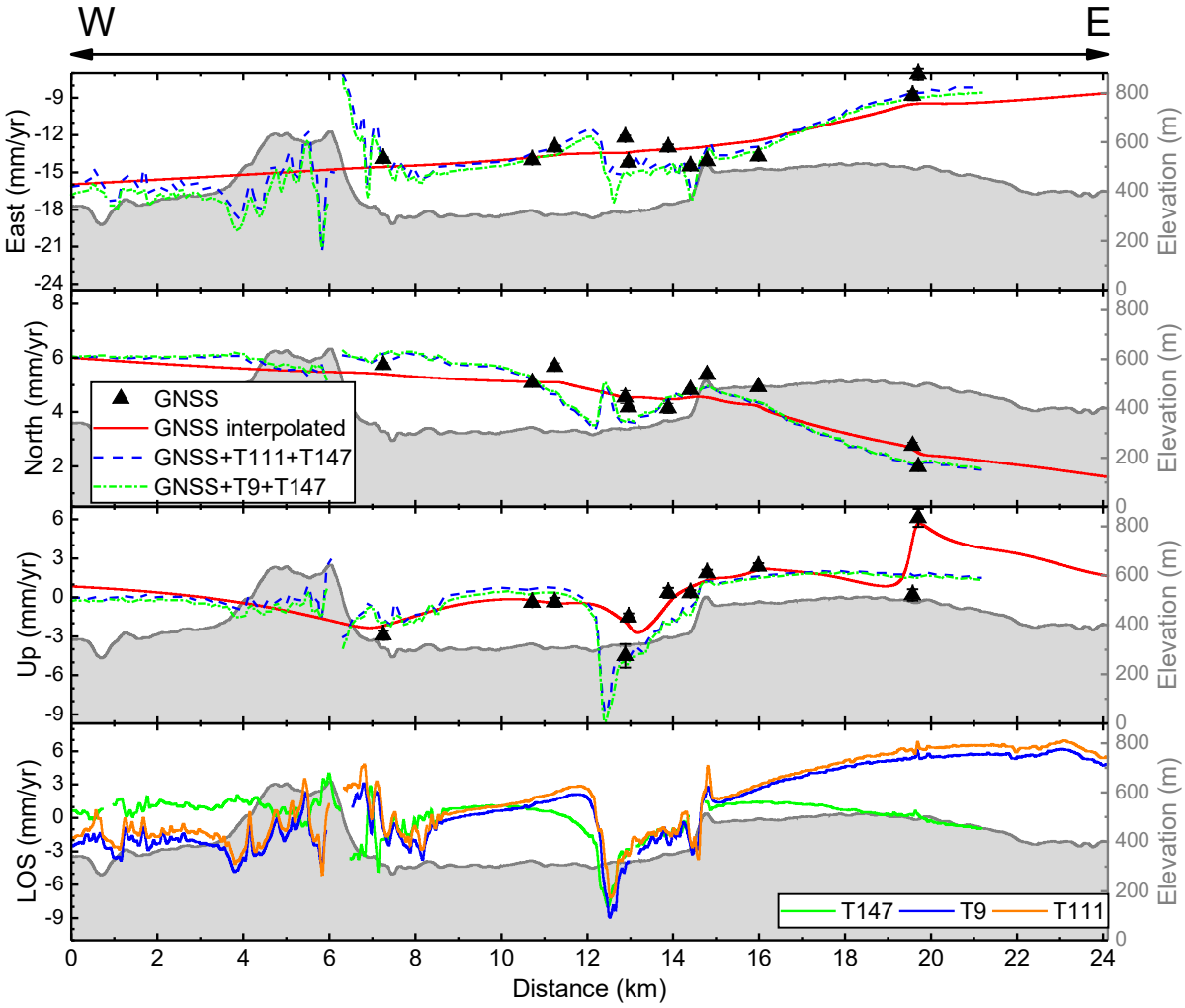

Figure 38. Central-north profile of long-term displacement in the Þeistareykir area. The triangles show the displacement velocities at near-by GNSS sites projected onto the profile at the same longitude. GNSS interpolated, GNSS+T111+T147, and GNSS+T9+T147 are profiles extracted from corresponding maps. The GNSS site names from west to south are TR04, THRC, TR44, TRG1, THER, TRG2, TR12, TR24, BOND, SANF, and TR26.

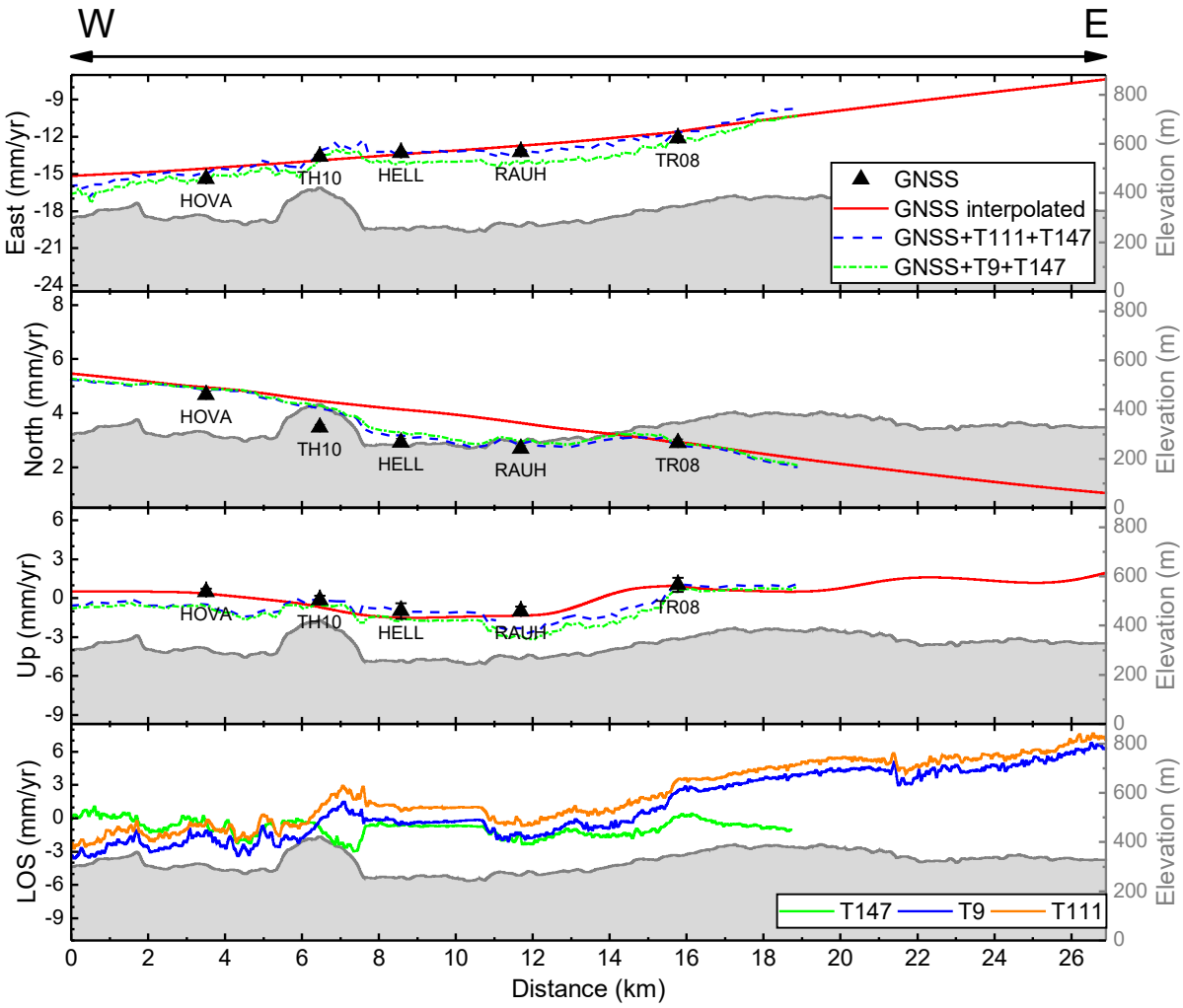

Figure 39. North profile of long-term displacement in the Þeistareykir area. The triangles show the displacement velocities at near-by GNSS sites projected onto the profile at the same longitude. GNSS interpolated, GNSS+T111+T147, and GNSS+T9+T147 are profiles extracted from corresponding maps.

Table 1. Estimated velocity of ground displacements at GNSS sites. The velocities are referred to Eurasian plate based on the ITRF2014 plate motion model (Altamimi et al., 2017). The unit of velocities and uncertainties are mm/yr. Span indicates the data used for velocity estimation. North, East and South indicate the velocities in corresponding components. Un_North, Un_East and Un_Up indicate the uncertainties of the velocities in corresponding components. See the text for GNSS time series analysis strategy.

Site	North	Un_North	Span	East	Un_East	Span	Up	Un_Up	Span
1008	7.78	0.05	2004–2023.9	-17.10	0.06	2004–2023.9	2.44	0.66	2004–2023.9
ADDA	6.87	0.15	2002–2013.9	-18.20	0.24	2002–2013.9	2.27	2.47	2002–2013.9
AMTM	1.66	0.05	2013–2023.9	-5.88	0.08	2013–2023.9	4.88	0.20	2013–2023.9
ARHO	3.40	0.01	2012–2023.9	-10.30	0.01	2012–2023.9	-1.21	0.02	2012–2023.9
AUDB	3.82	0.22	2002–2018.9	-11.00	0.11	2002–2018.9	0.34	0.92	2002–2018.9
AUSB	1.02	0.03	2002–2023.9	-3.77	0.09	2002–2023.9	4.65	0.20	2002–2023.9
AUSH	3.87	0.09	2012–2023.9	-9.22	0.15	2012–2023.9	2.58	0.32	2012–2023.9
BAUG	5.53	0.01	2012–2023.9	-14.40	0.01	2012–2023.9	-1.68	0.03	2012–2023.9
BF01	7.62	0.13	2012–2023.9	-10.60	0.12	2012–2023.9	-1.14	0.58	2012–2023.9
BF02	8.64	0.34	2012–2017.9	-12.70	0.53	2012–2017.9	4.05	1.65	2012–2017.9
BF03	8.15	0.32	2012–2017.9	-12.00	0.45	2012–2017.9	4.81	2.14	2012–2017.9
BF04	8.38	0.41	2012–2018.9	-12.30	0.36	2012–2018.9	-1.47	2.14	2012–2018.9
BF05	7.51	0.32	2012–2017.9	-12.40	0.29	2012–2017.9	-3.36	1.24	2012–2017.9
BF09	6.70	0.13	2012–2023.9	-10.20	0.15	2012–2023.9	-0.01	1.06	2012–2023.9
BF10	6.95	0.16	2012–2021.9	-9.39	0.11	2012–2021.9	-0.12	0.57	2012–2021.9
BF11	4.43	0.22	2012–2021.9	-10.30	0.51	2012–2021.9	1.90	0.65	2012–2021.9
BF12	6.42	0.31	2012–2017.9	-9.18	0.49	2012–2017.9	5.43	2.72	2012–2017.9
BF13	4.26	0.22	2012–2023.9	-9.93	0.14	2012–2023.9	0.67	0.52	2012–2023.9
BF18	6.75	0.11	2012–2023.9	-11.80	0.09	2012–2023.9	-1.08	0.62	2012–2023.9
BF20	4.70	0.16	2016–2023.9	-10.90	0.12	2016–2023.9	-3.83	0.82	2016–2023.9
BJAC	7.22	0.01	2012–2023.9	-11.50	0.01	2012–2023.9	-1.63	0.03	2012–2023.9

(continued)

BLAS	2.64	0.10	2013–2022.9	-11.80	0.14	2013–2022.9	1.19	0.30	2013–2022.9
BOND	4.93	0.03	2010–2022.9	-13.70	0.04	2010–2022.9	2.39	0.23	2010–2022.9
BOTF	3.98	0.18	2012–2023.9	-10.30	0.23	2012–2023.9	0.17	0.44	2012–2023.9
EILI	0.24	0.07	2005–2023.9	-5.54	0.11	2013–2023.9	6.33	0.30	2005–2023.9
ELDA	6.24	0.23	2012–2016.9	-10.50	0.28	2012–2016.9	-1.56	1.40	2012–2016.9
FM15	5.32	0.12	2013–2023.9	-11.60	0.11	2013–2023.9	-0.27	0.41	2013–2023.9
GAES	1.49	0.20	2002–2011.9	-7.55	0.14	2002–2011.9	5.66	0.75	2002–2011.9
GAKE	1.96	0.03	2010–2019.9	-7.86	0.03	2010–2019.9	-0.17	0.11	2010–2019.9
GDAL	5.91	0.23	2013–2017.9	-14.10	0.30	2013–2017.9	13.40	2.16	2013–2017.9
GEIF	6.87	0.06	2008–2023.9	-17.20	0.08	2008–2023.9	1.27	0.42	2008–2023.9
GJAV	0.83	0.10	2005–2023.9	-8.94	0.15	2005–2023.9	1.48	0.57	2013–2023.9
GRAN	6.41	0.01	2006–2016.9	-18.10	0.02	2006–2016.9	0.37	0.06	2006–2016.9
GRJO	0.11	0.08	2005–2019.9	-7.91	0.18	2005–2019.9	5.34	0.40	2005–2019.9
HAMH	6.13	0.11	2002–2022.9	-15.60	0.12	2002–2022.9	2.97	0.30	2002–2022.9
HAST	1.11	0.05	2002–2023.9	-2.44	0.11	2013–2023.9	2.76	0.26	2013–2023.9
HEDI	4.70	0.01	2008–2012.9	-12.80	0.01	2008–2012.9	-1.72	0.03	2008–2012.9
HEHO	3.92	0.15	2002–2018.9	-11.40	0.11	2002–2018.9	0.85	0.27	2002–2018.9
HELL	2.93	0.14	2013–2022.9	-13.30	0.08	2002–2022.9	-0.98	0.60	2013–2022.9
HITR	6.53	0.06	2010–2023.9	-13.20	0.06	2010–2023.9	0.29	0.24	2010–2023.9
HOLL	3.17	0.13	2002–2018.9	-7.78	0.13	2002–2018.9	-4.84	0.44	2002–2018.9
HOTJ	3.95	0.01	2011–2023.9	-11.20	0.01	2011–2023.9	-1.98	0.03	2011–2023.9
HOVA	4.69	0.13	2013–2022.9	-15.40	0.10	2002–2022.9	0.49	0.25	2002–2022.9 2017excluded
HRHA	1.16	0.08	2002–2023.9	-10.20	0.12	2013–2023.9	0.04	0.25	2013–2023.9
HSHO	2.45	0.12	2002–2012.9	-6.89	0.16	2002–2012.9	5.68	0.40	2002–2023.9
HVIT	5.73	0.14	2002–2012.9	-11.10	0.08	2013–2022.9	0.10	0.43	2013–2022.9
HVRO	7.72	0.15	2012–2017.9	-12.80	0.21	2012–2017.9	-5.65	0.72	2012–2017.9

(continued)

K089	4.61	0.18	2012–2023.9	-11.40	0.12	2012–2023.9	-3.25	0.43	2012–2023.9
KB11	2.33	0.17	2013–2023.9	-7.17	0.11	2013–2023.9	0.24	0.66	2013–2023.9
KMDA	1.98	0.13	2015–2023.9	-7.12	0.21	2015–2023.9	-0.20	0.84	2015–2023.9
KMDB	1.15	0.18	2015–2023.9	-7.39	0.24	2015–2023.9	-0.23	0.79	2015–2023.9
KMDC	4.56	0.26	2015–2023.9	-7.65	0.29	2015–2023.9	-1.34	0.98	2015–2023.9
KRAC	3.64	0.02	2011–2023.9	-9.26	0.01	2011–2023.9	-0.91	0.03	2011–2023.9
KRAF	2.55	0.18	2002–2022.9	-11.50	0.14	2002–2022.9	-0.16	0.39	2002–2022.9
KROV	3.89	0.12	2012–2023.9	-11.10	0.11	2012–2023.9	2.51	0.37	2012–2023.9
KV20	3.24	0.14	2013–2023.9	-8.02	0.14	2013–2023.9	-0.29	0.77	2013–2023.9
KVIH	5.16	0.08	2010–2021.9	-14.20	0.13	2010–2021.9	2.50	0.51	2010–2021.9
KVIS	4.62	0.01	2002–2023.9	-12.80	0.01	2002–2023.9	-1.38	0.02	2002–2023.9
L102	5.65	0.16	2013–2023.9	-11.90	0.15	2013–2023.9	-3.23	0.36	2013–2023.9
L111	2.87	0.07	2013–2023.9	-8.55	0.18	2013–2023.9	1.19	0.30	2013–2023.9
L113	2.24	0.11	2013–2019.9	-9.56	0.13	2013–2019.9	3.77	0.59	2013–2019.9
L119	4.87	0.06	2012–2023.9	-9.13	0.06	2012–2023.9	-1.99	0.16	2012–2023.9
L123	5.71	0.15	2012–2019.9	-11.30	0.14	2012–2019.9	-0.76	0.63	2013–2019.9
L157	3.25	0.16	2012–2023.9	-10.20	0.14	2012–2023.9	0.37	0.29	2012–2023.9
L205	7.63	0.17	2012–2018.9	-10.50	0.32	2012–2018.9	-1.30	1.48	2012–2018.9
L595	1.41	0.09	2013–2023.9	-6.72	0.15	2013–2023.9	-1.33	0.31	2013–2023.9
L597	3.47	0.21	2013–2023.9	-9.31	0.12	2013–2023.9	1.98	0.46	2013–2023.9
L598	3.87	0.24	2012–2023.9	-10.30	0.16	2012–2023.9	-0.31	0.62	2012–2023.9
L599	4.44	0.17	2012–2023.9	-10.40	0.11	2012–2023.9	-0.47	0.36	2012–2023.9
L603	7.33	0.16	2012–2023.9	-7.61	0.10	2012–2023.9	-8.73	2.07	2012–2023.9
L604	7.44	0.16	2012–2018.9	-7.97	0.43	2012–2018.9	-1.47	1.57	2012–2018.9
L671	2.24	0.17	2013–2023.9	-8.58	0.28	2013–2023.9	2.35	0.57	2013–2023.9
L673	4.61	0.18	2013–2023.9	-11.40	0.12	2013–2023.9	-3.25	0.43	2013–2023.9

(continued)

L678	4.07	0.15	2013–2023.9	-10.40	0.16	2013–2023.9	-0.12	0.58	2013–2023.9
L684	3.54	0.12	2013–2023.9	-10.10	0.19	2013–2023.9	1.94	0.31	2013–2023.9
L685	3.90	0.09	2013–2023.9	-10.10	0.17	2013–2023.9	1.36	0.44	2013–2023.9
L697	4.10	0.13	2012–2023.9	-11.00	0.10	2012–2023.9	0.12	0.42	2012–2023.9
L699	5.16	0.11	2011–2023.9	-11.50	0.09	2011–2023.9	-1.37	0.26	2011–2023.9
L842	9.31	0.23	2012–2018.9	-12.00	0.22	2012–2018.9	-0.08	0.56	2012–2018.9
LHSA	3.02	0.26	2019–2023.9	-7.59	0.26	2019–2023.9	-7.66	8.93	2019–2023.9
LV20	8.63	0.12	2011–2019.9	-11.70	0.14	2011–2019.9	-5.37	0.43	2011–2019.9
LYNG	2.14	0.13	2002–2018.9	-6.39	0.17	2002–2018.9	0.08	2.76	2002–2018.9
MIDA	0.95	0.05	2005–2023.9	-4.88	0.09	2013–2023.9	3.97	0.41	2013–2023.9
MULA	6.94	0.04	2002–2019.9	-7.94	0.07	2002–2019.9	0.37	0.20	2002–2019.9
MYEL	1.08	0.10	2002–2023.9	-7.60	0.08	2002–2023.9	0.82	0.84	2013–2023.9
MYVA	6.28	0.00	2006–2023.9	-8.58	0.00	2006–2023.9	-0.51	0.01	2006–2023.9
MYVN	5.96	0.07	2002–2023.9	-9.77	0.10	2002–2023.9	1.02	0.33	2002–2023
NAMA	6.07	0.07	2012–2023.9	-11.80	0.09	2012–2023.9	-1.48	0.25	2012–2023.9
NOME	0.05	0.04	2002–2023.9	-1.29	0.08	2013–2023.9	4.75	0.15	2002–2023.9
NOMO	1.10	0.06	2002–2023.9	-7.70	0.20	2013–2023.9	1.06	0.48	2013–2023.9
RAHO	4.12	0.05	2002–2023.9	-6.09	0.05	2002–2023.9	-0.57	0.34	2013–2023.9
RAND	5.39	0.07	2013–2023.9	-14.60	0.07	2002–2023.9	4.34	0.19	2002–2023.9
RAUH	2.69	0.12	2013–2022.9	-13.20	0.14	2013–2022.9	-0.99	0.35	2013–2022.9
SAMD	2.47	0.08	2012–2023.9	-10.30	0.12	2012–2023.9	0.18	0.35	2012–2023.9
SAMU	0.80	0.12	2002–2013.9	-8.81	0.13	2002–2013.9	5.47	0.66	2002–2013.9
SANF	1.98	0.10	2006–2015.9	-7.09	0.43	2006–2015.9	6.13	0.69	2006–2015.9
SAVI	6.07	0.00	2007–2023.9	-15.50	0.01	2016–2023.9	-1.31	0.02	2007–2023.9
SJUK	5.28	0.01	2012–2023.9	-13.90	0.01	2012–2023.9	-1.47	0.03	2012–2023.9
SKHO	4.07	0.15	2010–2022.9	-10.40	0.16	2010–2022.9	-0.12	0.58	2010–2022.9

(continued)

SKIL	3.40	0.06	2010–2022.9	-13.90	0.03	2010–2022.9	-1.58	0.19	2013–2023.9
STOK	2.79	0.08	2002–2023.9	-8.89	0.09	2002–2023.9	2.29	0.41	2013–2023.9
T517	4.98	0.12	2012–2023.9	-11.40	0.10	2012–2023.9	-0.73	0.46	2012–2023.9
TABR	2.22	0.07	2007–2023.9	-5.58	0.10	2007–2023.9	4.67	0.25	2007–2023.9
TH10	3.48	0.10	2011–2022.9	-13.60	0.16	2011–2022.9	-0.13	0.33	2011–2022.9
TH17	4.04	0.06	2011–2023.9	-13.40	0.17	2011–2023.9	0.00	0.25	2011–2023.9
THER	4.18	0.06	2002–2023.9	-14.20	0.15	2013–2023.9	-1.52	0.31	2013–2023.9
THHY	3.30	0.18	2013–2023.9	-8.59	0.11	2013–2023.9	-1.49	0.45	2013–2023.9
THRC	5.09	0.01	2011–2023.9	-14.00	0.01	2011–2023.9	-0.39	0.03	2011–2023.9
TR04	5.74	0.10	2011–2021.9	-13.90	0.13	2011–2021.9	-2.91	0.34	2011–2021.9
TR08	2.91	0.13	2011–2022.9	-12.10	0.13	2011–2022.9	1.02	0.54	2011–2022.9
TR10	3.85	0.13	2011–2021.9	-13.10	0.33	2011–2021.9	0.69	0.96	2011–2021.9
TR11	3.94	0.15	2011–2021.9	-13.80	0.21	2011–2021.9	-1.90	0.63	2011–2021.9
TR12	4.83	0.07	2011–2022.9	-14.50	0.13	2011–2022.9	0.33	0.23	2011–2022.9
TR14	3.60	0.13	2011–2020.9	-14.60	0.10	2011–2020.9	-1.71	0.32	2011–2020.9
TR15	7.29	0.07	2011–2022.9	-13.40	0.06	2011–2022.9	2.23	0.31	2011–2022.9
TR16	6.84	0.10	2011–2022.9	-14.50	0.13	2011–2022.9	2.56	0.18	2011–2022.9
TR20	7.28	0.28	2011–2019.9	-16.00	0.18	2011–2019.9	2.51	0.47	2011–2019.9
TR23	6.83	0.10	2011–2022.9	-14.90	0.11	2011–2022.9	0.57	0.28	2011–2022.9
TR24	5.38	0.08	2011–2023.9	-14.10	0.11	2011–2023.9	1.88	0.23	2011–2023.9
TR26	2.76	0.13	2011–2019.9	-8.81	0.35	2011–2019.9	0.20	0.45	2011–2019.9 2017excluded
TR29	1.58	0.16	2011–2018.9	-8.59	0.18	2011–2018.9	4.02	1.60	2011–2018.9
TR32	2.71	0.06	2011–2023.9	-9.69	0.10	2011–2023.9	1.91	0.28	2011–2023.9
TR34	4.21	0.11	2011–2021.9	-13.00	0.10	2011–2021.9	2.77	0.41	2011–2021.9
TR37	4.07	0.18	2011–2019.9	-11.70	0.50	2013–2019.9	3.60	0.41	2011–2019.9

(continued)

TR39	2.30	0.22	2011–2015.9	-10.40	0.31	2011–2015.9	0.13	1.17	2011–2015.9
TR41	5.94	0.17	2013–2018.9	-15.50	0.23	2013–2018.9	6.71	1.42	2013–2018.9
TR44	5.68	0.13	2015–2022.9	-13.00	0.16	2015–2022.9	-0.37	0.35	2015–2022.9
TR46	4.36	0.18	2015–2020.9	-12.60	0.15	2015–2020.9	0.00	0.72	2015–2020.9
TRG1	4.55	0.23	2017–2023.9	-12.20	0.17	2017–2023.9	-4.49	0.91	2017–2023.9
TRG2	4.14	0.19	2017–2023.9	-13.00	0.26	2017–2023.9	0.37	0.38	2017–2023.9
VIDA	7.69	0.10	2013–2023.9	-15.70	0.21	2013–2023.9	1.91	0.30	2013–2023.9
VITI	0.97	0.07	2002–2023.9	-9.17	0.08	2002–2023.9	1.38	0.42	2013–2023.9
VR71	6.75	0.13	2012–2023.9	-12.40	0.10	2012–2023.9	2.09	0.37	2012–2023.9 2017excluded

Table 2. Coordinates of profiles across the Þeistareykir area.

Profile	West endpoint		East endpoint	
	Longitude	Latitude	Longitude	Latitude
South	-17.2391°	65.8087°	-16.8448°	65.7691°
Central-south	-17.2561°	65.8605°	-16.7629°	65.8137°
Central-north	-17.2400°	65.9124°	-16.7265°	65.8577°
North	-17.2238°	65.9653°	-16.6494°	65.9049°

References

Altamimi Z, Métivier L, Rebischung P, et al. (2017). ITRF2014 plate motion model. 209(3), 1906–1912.

Árnason K. (2020). New Conceptual Model for the Magma-Hydrothermal-Tectonic System of Krafla, NE Iceland. Geosciences, 10(1), 34.

Blewitt G, & Lavallée D. (2002). Effect of annual signals on geodetic velocity. Journal of Geophysical Research: Solid Earth, 107(B7), ETG9-1–ETG9-11.

Drouin V, Sigmundsson F, Ófeigsson BG, et al. (2017). Deformation in the Northern Volcanic Zone of Iceland 2008–2014: An interplay of tectonic, magmatic, and glacial isostatic deformation. Journal of Geophysical Research: Solid Earth, 122(4): 3158–3178.

Drouin V. (2023). InSAR monitoring of Krafla, Bjarnarflag and Þeistareykir geothermal areas (2022 update). Landsvirkjun, LV-2023-005.

Freymueller J. (2017). Geodynamics. In: Teunissen, P.J., Montenbruck, O. (eds) Springer Handbook of Global Navigation Satellite Systems. Springer Handbooks. Springer, Cham.

Gudnason EA, Drouin V, Yang Y, et al. (2024). Changes in seismicity and observed deformation related to inflation at the Theistareykir high-temperature geothermal field, NE Iceland, in 2023–2024. EGU General Assembly 2024, Vienna, Austria.

Guglielmino F, Nunnari G, Puglisi G, et al. Simultaneous and Integrated Strain Tensor Estimation From Geodetic and Satellite Deformation Measurements to Obtain Three-Dimensional Displacement Maps. IEEE Transactions on Geosciecne and Remote Sensing, 49(6), 1815–1826.

Hjartardóttir AR, Einarsson P, Magnúsdóttir S, et al. (2015). Fracture systems of the Northern Volcanic Rift Zone, Iceland: an onshore part of the Mid-Atlantic plate boundary. Geological Society, London, Special Publications, 420, 297–314.

Kim D, Brown LD, Árnason K, et al. (2020). Magma “bright spots” mapped beneath Krafla, Iceland, using RVSP imaging of reflected waves from microearthquakes. Journal of Volcanology and Geothermal Research, 391, 106365.

LMI. (2022). ÍslandsDEM útgáfa 1.0. Landmaelingar Íslands. Available at https://www.lmi.is/is/umlmi/frettayfirlit/ny-uppfaersla-a-haedarlikani-af-islandi.

Lanzi C, Sigmundsson F, Geirsson H, et al. (2022). 2021 GNSS surveying and surface deformation at Krafla, Námafjall and Þeistareykir. Landsvirkjun, LV-2022-027.

Sandwell DT, & Wessel P. (2016). Interpolation of 2-D vector data using constraints from elasticity. Geophysical Research Letters, 43(20), 703–710.

Shen Z-K, Wang M, Zeng Y, et al. (2015). Optimal Interpolation of Spatially Discretized Geodetic Data. Bulletin of the Seismological Society of America, 105(4), 2117–2127.

Tryggavason E. (1984). Widening of the Krafla Fissure Swarm During the 1975–1981 Volcano-tectonic Episode. Bulletin of Volcanology, 47(1), 47–69.

Yang Y, Lanzi C, Sigmundsson F, et al. (2023). 2022 GNSS surveying and ground deformation at Krafla, Námafjall and Þeistareykir. Landsvirkjun, LV-2023-034.